

Article

Feasibility Study for Sustainable Use of Lithium-Ion Batteries Considering Different Positive Electrode Active Materials under Various Driving Cycles by Using Cell to Electric Vehicle (EV) Simulation

Heewon Choi ¹, Nam-gyu Lim ¹, Seong Jun Lee ² and Jungsoo Park ^{2,*}

¹ Department of Mechanical Engineering, Graduate School, Chosun University, Gwangju 61452, Korea; hwchoi0924@gmail.com (H.C.); lnk9100@chosun.ac.kr (N.-g.L.)

² Department of Mechanical Engineering, Chosun University, Gwangju 61452, Korea; lsj@chosun.ac.kr

* Correspondence: j.park@chosun.ac.kr

Received: 16 October 2020; Accepted: 19 November 2020; Published: 23 November 2020



Abstract: Electric vehicles have been issued to achieve sustainable mobility. Main factors to sustainable electric vehicle (EV) are that lithium-ion battery (LIB) has to maintain lower cost, lighter weight, SOC (state of charge), thermal stability, and driving ranges. In this study, nickel-cobalt-manganese (NCM), lithium iron phosphate (LFP), and lithium manganese oxide (LMO), which are used as representative positive electrode materials, were applied to battery cells. Then, the battery characteristics at the system level, according to the application of different positive electrode materials, were compared and analyzed. To this end, each of the 18650 cylindrical battery cells was modeled by applying different positive electrode active materials. The battery modeling was based on a database provided by GT(Gamma Technologies)-AutoLion. To analyze the thermal stability and capacity loss according to the temperature of the battery cell by applying different C-rate discharge and temperature conditions for each positive electrode active material, an electrochemical-based zero-dimensional (0D) analysis was performed. A test was also performed to determine the model feasibility by using a MACCOR 4300 battery charger/discharger. Moreover, a lumped battery pack modeling was performed to extend the modeled battery cell to an EV battery pack. By combining the pack and one-dimensional (1D) EV models, various driving cycles were described to investigate the battery performance at the vehicle level. It was found that the 0D electrochemistry-coupled 1D vehicle model could well predict the feasible tendencies considering various positive electrode materials of the LIB battery cell.

Keywords: lithium-ion battery; AutoLion; positive electrode material; electric vehicle

1. Introduction

Since the importance of secondary batteries has been highlighted along with the possibility of applications in electric vehicles (EVs) and energy storage systems (ESSs), various studies have been conducted to improve the efficiency of lithium-ion batteries (LIBs). In particular, the positive electrode material, which is the core component of LIBs, has the highest development cost and determines the charging and discharging performances of batteries. Therefore, extensive research has been conducted to optimize this material according to EV or power system specifications.

The well-known LIB positive electrode materials are typically nickel cobalt manganese (NCM) with layered structure, lithium manganese oxide (LMO) with spinel structure, and lithium iron phosphate (LFP) with olivine structure. Research on battery performances using these positive electrode active materials has been actively conducted. The layered structure of NCM has been investigated for its

electrochemical performance and thermal stability according to NCM content by Jiang et al. [1,2]. Electrochemical, calorimeter, nail penetration, and heating tests for NCM 523, NCM 622, and NCM 811 were performed. The results showed that the NCM 622 material has good compatibility with NCM 523 and NCM 811. LFP uses environmentally friendly iron instead of Co, which is mainly used as a positive electrode active material. LFP has the advantages of low cost, excellent life characteristics, and safety; however, it has the disadvantage of low electronic conductivity. Research is being conducted to improve its electrochemical performance through doping and nanoparticle formation, as well as with the use of a carbon coating on the particle surface [3]. LMO also has advantages, such as low price, eco-friendliness, structural stability, and high operating voltage, while it has the disadvantage of capacity reduction due to structural instability and Mn elution at high temperatures [4]. To overcome the advantages and disadvantages of these positive electrode active materials, an approach using heterogeneous materials is also being attempted [5,6]. Ku et al. reported that the electrochemical performance characterization of layered-spinel, hetero-structured, positive electrode materials could be improved with respect to higher initial Coulombic efficiency, larger specific capacity, and better cycling and rate properties [6].

However, most of these studies were conducted in limited test environments to obtain the quantitative results, and most of the characteristics were investigated at the cell level. To overcome the limitations of these experimental studies, numerical approaches have been developed. In particular, owing to the complex phenomena of LIBs, including the electro-chemo-mechanics, many studies have been conducted to investigate the complex behavior considering their material characteristics [7]. Many researchers have attempted to validate the diffusion-induced stress and stress-induced diffusion phenomena based on particle simulations of the active material itself at the particle level [8–10]. In addition, modeling studies of the lithiation and delithiation phenomena have been conducted, focusing on the structural aspects of the positive electrode active material considering heat and mass transfer [11], phase transformation [12], and the degradation mechanism [13]. At the composite electrode level, research has been conducted in terms of particle–particle, particle–matrix, and particle–electrolyte interactions [14,15].

Particle and composite models have been used for cell-level model implementation, and research has been conducted on two-dimensional (2D)/three-dimensional (3D) cell models [16–18]. These studies imply that cell models are very important because their outcomes can be directly compared with experimental measures, which offer optimization criteria for the electrodes and electrolyte.

Most of these modeling studies were approached from a material viewpoint. However, to be integrated into an EV or power system through the battery pack, a macro-scale analysis is required. From this point of view, building the model while covering all the modeling from the component level to system level is a factor that maximizes the benefit of the cost of time if system integration is considered. In particular, for a 3D analysis capable of detailed modeling, most of the research has been conducted on thermal models excluding electrochemistry [19,20]. In addition, in some studies, a simplified electrochemical model was implemented; however, these models have limitations in that they can be applied only to the cell level to which the positive electrode active material of the study is applied. They are not commonly applied to NCM, LFP, and LMO through normalizing the dominant parameters.

The above research was been focused on the bottom-up design approach for battery cell. However, considering that the LIB is usually installed in the EV system in the form of a battery pack and exposed to the hard-driving environment, it will be helpful to investigate sustainability by first checking feasibility when applied to the EV performing top-down cell design. In that point of view, this study focused on proving reverse calibration method and fast design processes of LIB using LIB design tools, although there was lack of model calibration processes. As the first step, the present study aimed for identification of feasibility over accurate calibration by comparing the minimum available experimental data and raw simulation data without parameter tune. Therefore, typical tuning parameters, such as N/P ratio (areal capacity ratio of negative to positive electrode), OCV (open circuit

voltage) limit value, capacity loading value, heat transfer coefficient, etc., are used for model calibration when battery information is unknown. In this study, NCM-based 1D electrochemical model was expanded and applied to LFP- and LMO-based models to determine the feasibility of predicting battery cell performance based on various positive electrode active materials. Cell performance from simulation was basically compared to test data of NCM battery cell with unknown physical properties. Expanding the model from a cell to an EV system, the prediction feasibility was introduced for the 1D LIB electrochemical model from a macroscopic point of view.

2. Methodologies

2.1. Battery Cell and Pack Simulation

2.1.1. Governing Equations for Electrochemistry and Thermally Coupled Battery Model

To consider the chemical properties inside a battery, a battery cell was modeled using GT-AutoLion, a LIB simulation software. The internal electrochemical reaction of the battery cell was calculated using the governing equation shown as follows referred to as a pseudo-two-dimensional model:

$$0 = \frac{\partial}{\partial x} \left(\sigma_s^{eff} \frac{\partial \Phi_s}{\partial x} \right) - j^{Li} - a_{dl} c \frac{\partial (\Phi_s - \Phi_e)}{\partial x} \quad (1)$$

$$0 = \frac{\partial}{\partial x} \left(k^{eff} \frac{\partial \Phi_e}{\partial x} \right) - \frac{\partial}{\partial x} \left(k_D^{eff} \frac{\partial \ln c_e}{\partial x} \right) + j^{Li} + a_{dl} c \frac{\partial (\Phi_s - \Phi_e)}{\partial x} \quad (2)$$

$$\frac{\partial}{\partial t} [\varepsilon c_e] = \frac{\partial}{\partial x} \left(D_e^{eff} \frac{\partial c_e}{\partial x} \right) + \frac{1 - t_+^0}{F} j^{Li} \quad (3)$$

$$\frac{\partial c_s}{\partial t} = \frac{1}{r^2} \frac{\partial}{\partial r} \left(D_s r^2 \frac{\partial c_s}{\partial r} \right) \quad (4)$$

Equations (1) and (2) represent the charge conservation in the solid phase and electrolyte. The charge conservation in solid phase, Φ_s , is dependent upon the conductivity of solid phase, σ_s , and reaction current density, j^{Li} . The electrolyte phase charge conservation, Φ_e , is affected by ionic conductivity, k_{eff} .

Equation (3) provides Li-ion concentration profile in the liquid phase, depending on the effective diffusivity in the electrolyte as D_e^{eff} , the porosity as ε , current density as j^{Li} , and the Li-ion transference number as t_+^0 . Equation (4) represents distribution of Li in the spherical particles occupied in each control volume of the electrodes, where c_s is the Li-ion concentration, D_s is the solid phase diffusion coefficient, and r is the radius.

Throughout the above calculations, according to each positive electrode active material properties, state of charge can be estimated by the following equations [21]:

$$SOC(t) = \frac{SOC_{init} \times Capacity - \int_0^t I_{OC} dt}{Capacity} \quad (5)$$

where SOC_{init} is initial SOC (state of charge), $Capacity$ is desired capacity with different materials, and I_{OC} is open circuit current. These setup values are discussed in Section 2.1.2.

The thermal model used in this study can be coupled with P2D (pseudo-two-dimensional) model referred to as thermal-coupled battery model, TCB. The lumped energy conservation is applied to correlate cell temperature, T , to the generated heat inside the cell and the convective dissipated heat to the ambient as follows [22,23]:

$$\frac{d(\rho c_p T)}{dt} = -h A_s (T - T_\infty) + Q_{gen} \quad (6)$$

where h is the convection heat transfer coefficient, T_∞ is the cooling medium temperature, A_s is the cell outer surface area, and Q_{gen} is the total heat generated within the cell having summation forms of Joule heating, reaction heat, entropic heating, and heating due to contact resistance between the current collector and electrode materials [23].

Based on the governing equations, battery cell performance was calculated according to cell setup below.

2.1.2. Battery Cell Setup

The P2D model explained in Section 2.1.1. uses a finite control volume method and models Equations (1)–(4), which are the dominant equations of the battery cell, by discretizing them. Equations (1)–(3) are discretized in the thickness direction between the positive electrode and negative electrodes, and Equation (4) is discretized in a constant volume, as shown in Figure 1, in the radial direction of the active material particles. Table 1 summarizes the number of elements that were discretized when constructing the battery cell model.

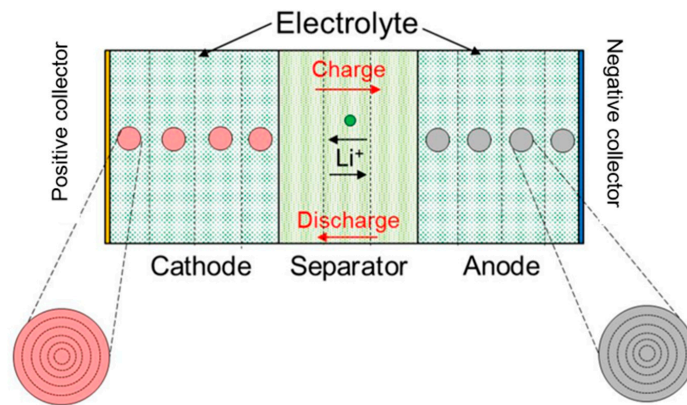


Figure 1. Battery cell discretization direction (thickness and radial direction) [21].

Table 1. Battery cell discretization.

Cell Discretization	Number of Elements
Positive electrode	6
Separator	4
Negative electrode	6
Positive electrode particle	12
Negative electrode particle	12

Using the electrochemical database provided by GT-AutoLion, a constant current discharge test of the battery cells for each positive electrode material was conducted, as shown in Figure 2.

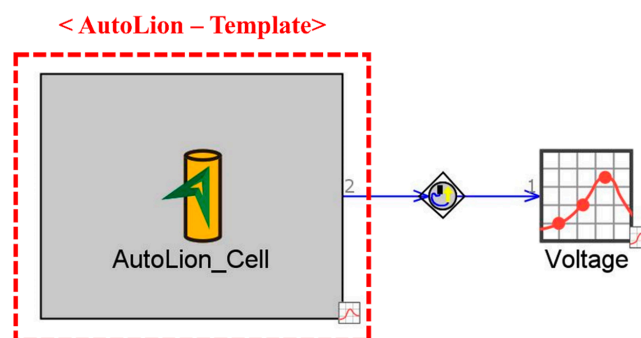


Figure 2. Battery cell CC(constant current)-discharge test setup.

When building the battery model, the input parameters needed for the analysis were set in the AutoLion template, as shown in Tables 2 and 3. To compare and analyze the effects of temperature and C-rate during the battery cell discharge, an analysis was performed using a 18650-type cylindrical battery. The battery performance was analyzed according to the application of the positive electrode active material through a 1 C-rate discharge at five temperature conditions (−20, −10, 0, 25, and 45 °C) and discharge tests according to different C-rates (0.2–5 C-rates) at 25 °C of room temperature by applying four types of positive electrode active materials (NCM 622, NCM 811, LFP, and LMO) to the battery cells. The initial SOC (state of charge) of the battery was set at 100%, and it was assumed that the ambient and initial temperatures were the same to simplify the TCB. Natural convection conditions ($h = 10 \text{ W/m}^2\cdot\text{K}$) were applied to the TCB.

Table 2. Battery cell material properties.

Positive Electrode		Negative Electrode	
Foil		Foil	
Material	Aluminum	Material	Copper
Thickness	15 μm	Thickness	8 μm
Active Material		Active Material	
Material	NCM/LFPO/LMO	Material	Graphite
Density	4.8/3.6/4.28 g/cm^3	Density	2.24 g/cm^3
Weight Percentage	94%	Weight Percentage	94%
Conductive Agent		Conductive Agent	
Material	Carbon	Material	Carbon
Weight Percentage	3%	Weight Percentage	3%
Binder		Binder	
Material	PVdF	Material	PVdF
Weight Percentage	3%	Weight Percentage	3%

Table 3. Battery cell specifications and operating conditions.

Type	Cylindrical
Diameter	18 mm
Height	65 mm
Positive electrode active material	NCM622/NCM811/LFP/LMO
Negative electrode active material	Graphite
Capacity	2.2/2.1/1.4/1.5 Ah
Discharge cutoff voltage	2.5 V
Charge cutoff voltage	4.2/4.2/3.65/4.2 V

2.1.3. Battery Pack Determination

The battery cell model analyzed above was expanded to a battery pack model mounted on the EV. The analysis was conducted at 25 °C, the environmental temperature at which the battery could perform optimally. When modeling the battery pack, the analysis was performed using the lumped battery pack model option provided by GT-AutoLion. Therefore, this study assumed that all battery cells had the same current, voltage, and temperature because the battery system was uniform. The number of serial cells required for the construction of the battery pack was calculated using Equation (7), and the total energy of the battery pack was calculated using Equation (8).

$$\text{Number of series cells} = V_p/V_c \quad (7)$$

$$E_p = V_p \times I_p \quad (8)$$

For the information on the voltage (V_c) of the battery cell and the voltage (V_p) and pack capacity (I_p) of the battery cell in Ah according to each positive electrode active material, the values from an analysis of the battery cell were used. The initial SOC condition of the battery pack was set to 80%. In accordance with the total battery energy (55 kWh) of the target EV specification, battery cells with different positive electrode materials were expanded to the battery pack model. Table 4 summarizes the number of series and parallel cells of the battery pack for the EV according to the application of each positive electrode material.

Table 4. Number of cells in a 55-kWh battery pack for the EV.

Positive Electrode Active Material	Number of Cells in Series	Number of Cells in Parallel
NCM622	100	70
NCM811	99	73
LFP	108	110
LMO	91	103

The manufactured battery model can be mounted on a system-level vehicle model to improve the reliability of the cell-level analysis through driving tests that reflect various environmental conditions. Many researchers have conducted research at the system level to obtain a higher reliability [23–25]. In this study, a 0-dimensional electrochemical model of the battery and a 1-dimensional vehicle model were coupled to perform an analysis at the system level. Figure 3 shows the EV model created by combining a battery pack made in GT-AutoLion with a 1D-based GT-Suite. The EV model consisted of a DC–DC converter, battery pack, motor, and vehicle, as shown in Figure 3.

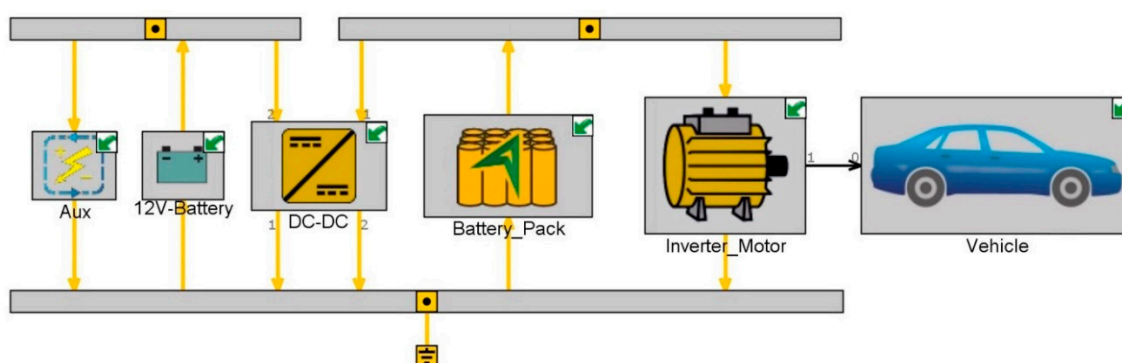


Figure 3. EV model with electrochemical battery pack from GT-AutoLion.

The model was constructed by physically connecting the templates of the elements constituting the above EV. The electrochemical battery model of the GT-AutoLion built for the target EV was constructed. Recently, to improve driving distances, the capacities of batteries mounted in EVs have been increased. In line with this trend, this study selected and analyzed the Tesla Model 3 (when equipped with a standard pack) and a high-capacity, 55-kWh battery model equivalent to Renault’s ZOE third generation, which is expected to be released in 2020. For this analysis, it was assumed that the environmental temperature was constant at 25 °C. Data for the components of the EV model were obtained from the database provided by GT and are summarized in Table 5. The constructed EV model applied four measurement methods: city driving mode (FTP-75, federal test procedure 75), highway driving mode (HWFET, highway fuel economy test), worldwide harmonized light-duty vehicle-test cycle (WLTC), and maximum and rapid deceleration driving mode (US06, United States 06), which measures fuel efficiency by assuming an environment similar to actual driving conditions. A battery pack, to which different positive electrode active materials were applied, was mounted on an EV model to compare battery performances and verify the reliability.

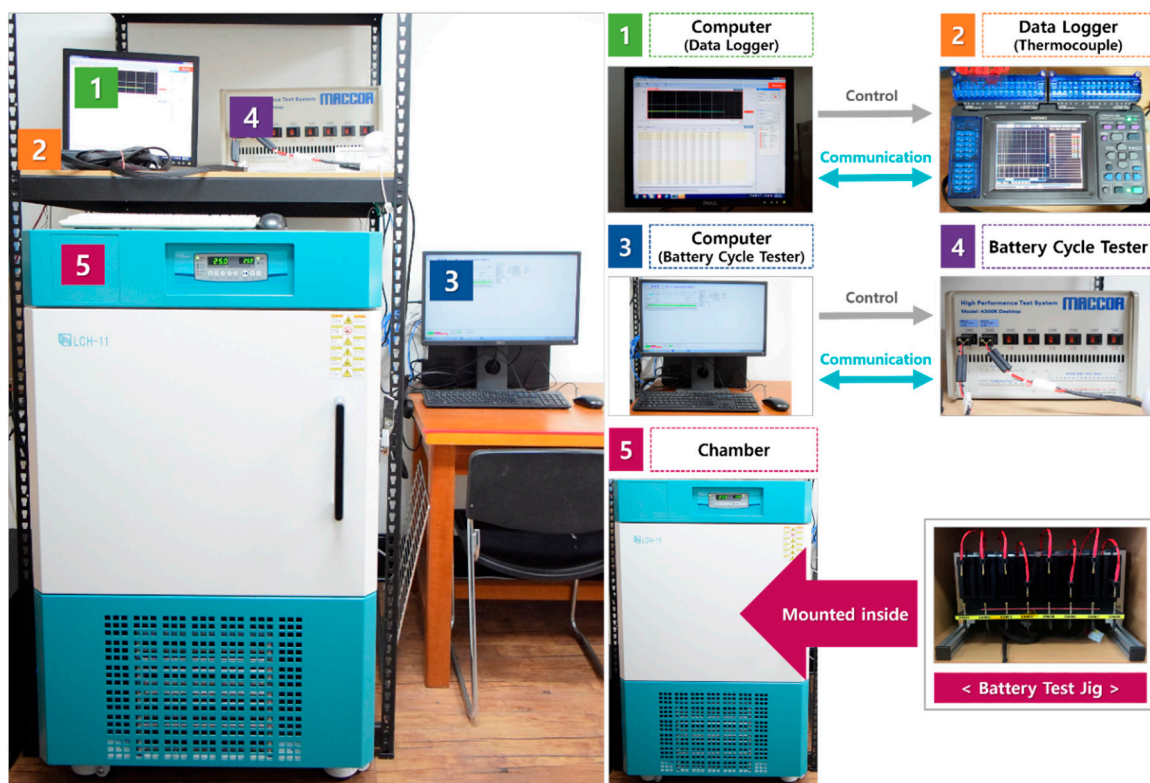
Table 5. EV model specifications [24].

Vehicle Mass	1600 kg
Vehicle Drag Coefficient	0.21
Vehicle Frontal Area	1.95 m ²
Tire Specification	215/50R17
Battery Pack Energy	55 kWh
Final Drive Ratio	7.05
Traction Motor Maximum Brake Torque	360 Nm
Traction Motor Maximum Efficiency	97%
Traction Motor Maximum Torque (Continuous)	300 Nm
Traction Motor Maximum Power	150 kW @ 4000 RPM

2.2. Battery Cell Experiment

2.2.1. Experimental Setup

In this study, a battery cell charging/discharging experiment was conducted using the equipment shown in Figure 4 to consider the temperature change and capacity loss of battery cells according to different C-rates.

**Figure 4.** Experimental setup.

In Figure 4, computer 1 is connected to data logger 2, which it can control, and is used to record and collect temperature data in real time. Computer 3 is connected to charging/discharging tester 4 and is used for setting and controlling the charging/discharging conditions, real-time monitoring, and collecting test result data. To perform the experiment at a constant temperature, a battery test jig was installed in chamber 5. All experiments were performed at room temperature, and the temperature was kept constant during the experiments.

Figure 5a shows a commercial 18650 cylindrical battery cell with a capacity of 2.5 Ah manufactured by LG-Chem. To measure the external surface temperature of the battery, a T-type thermocouple

mounted on the data logger was attached to the surface of the battery using Kapton tape, as shown in Figure 5b. The temperature was measured at a total of nine points by attaching the thermocouple to three points at the top, middle, and bottom [26] of the battery cell.

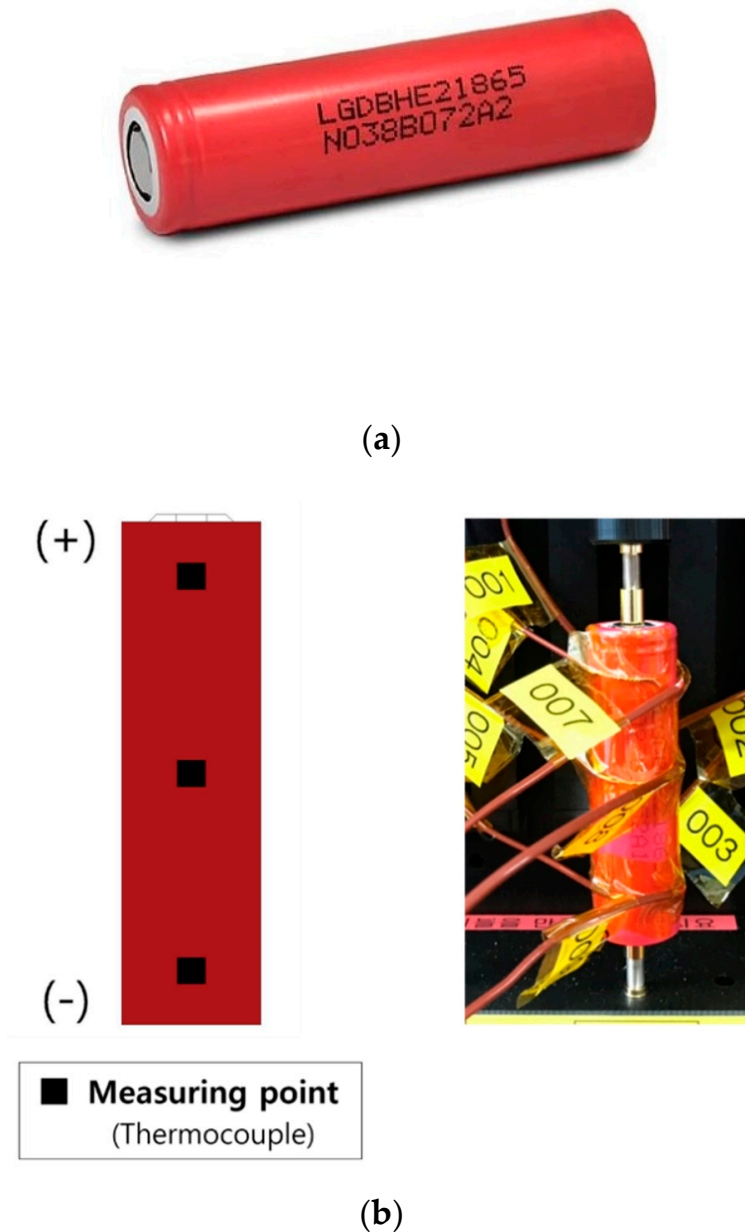


Figure 5. (a) 18650 cylindrical battery (LGDBHE21865). (b) Thermocouple attachment point for temperature measurement.

2.2.2. Experimental Method

Figure 6 shows a schematic diagram of the experimental process. First, to conduct a charge/discharge experiment on the battery cell, the battery was left in a chamber set to 25 °C, and the experiment was conducted when the set temperature was reached. Then, the rest time was set to 1 h to stabilize the battery cells. The constant current-constant voltage (CC-CV) method was used as the charging method. The initial stage of charging proceeded with a constant current (CC) charging method at a 0.5 C-rate until the upper cutoff voltage of 4.2 V was reached. Thereafter, the process proceeded with the constant voltage (CV) charging method, and when the current decreased to 0.05 A,

charging was terminated. At the end of the charging process, after 2 h of rest time, the discharge was terminated when the CC discharge proceeded at a 0.2 C-rate and reached the discharge cutoff voltage of 2.5 V, after which there were 2 h of rest time, similar to the charging process. In this way, experiments were performed in the order of 0.5, 1, and 2 C-rates. During the experiment, the rest time was set to 2 h after the charge/discharge process to sufficiently stabilize the temperature inside and outside of the battery, which increased due to the heat generated during the charge/discharge process. This experiment was repeated three times per battery cell, and the average value of the results obtained by performing a total of nine experiments was used.

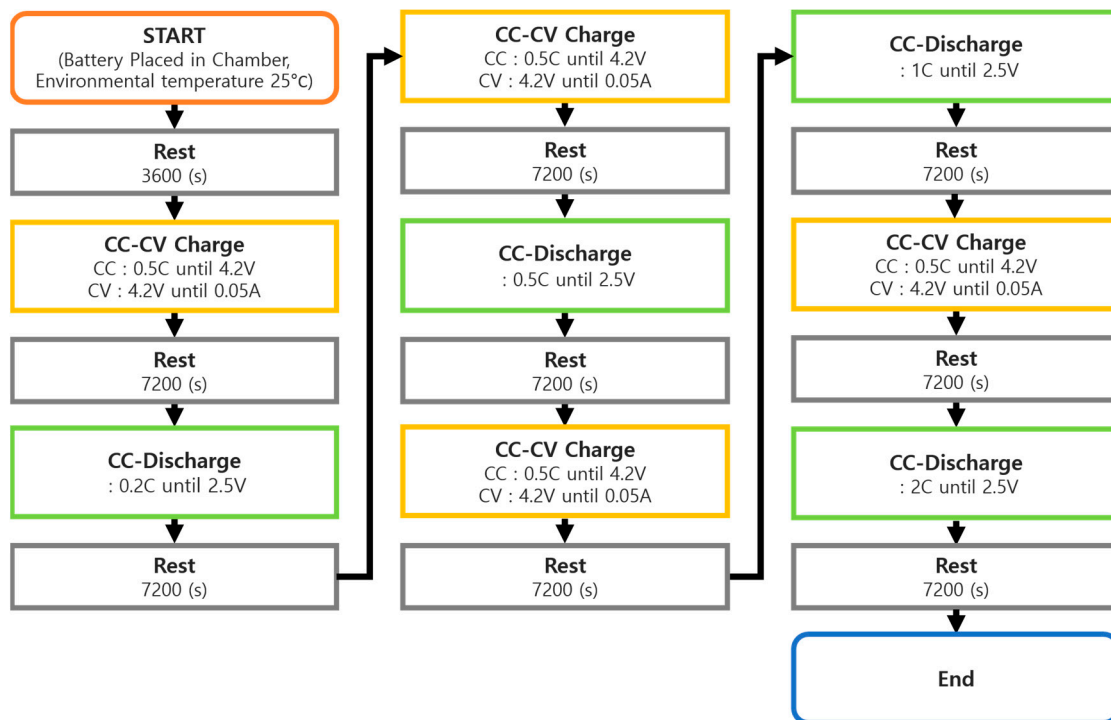


Figure 6. Battery cell charge and discharge test procedure (discharge at 0.2, 0.5, 1, and 2 C-rates).

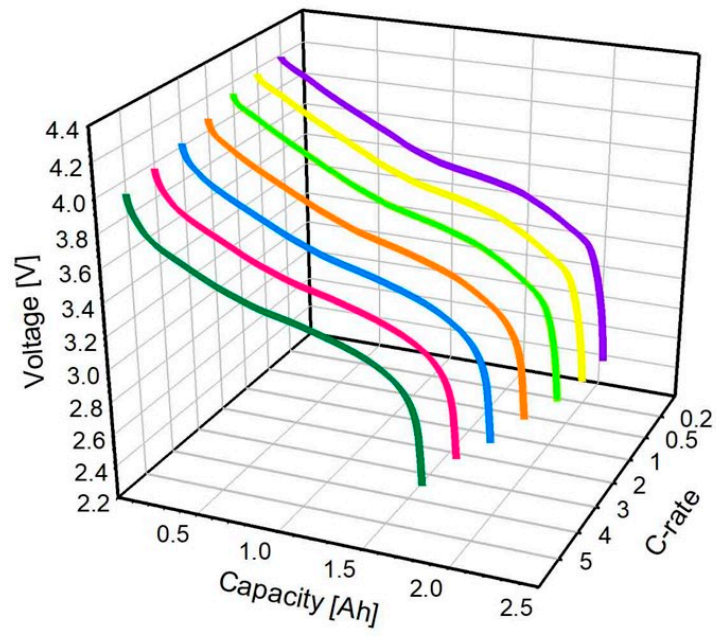
3. Results and Discussion

3.1. Analysis of Battery Cell Characteristics According to the Type of Positive Electrode Active Material

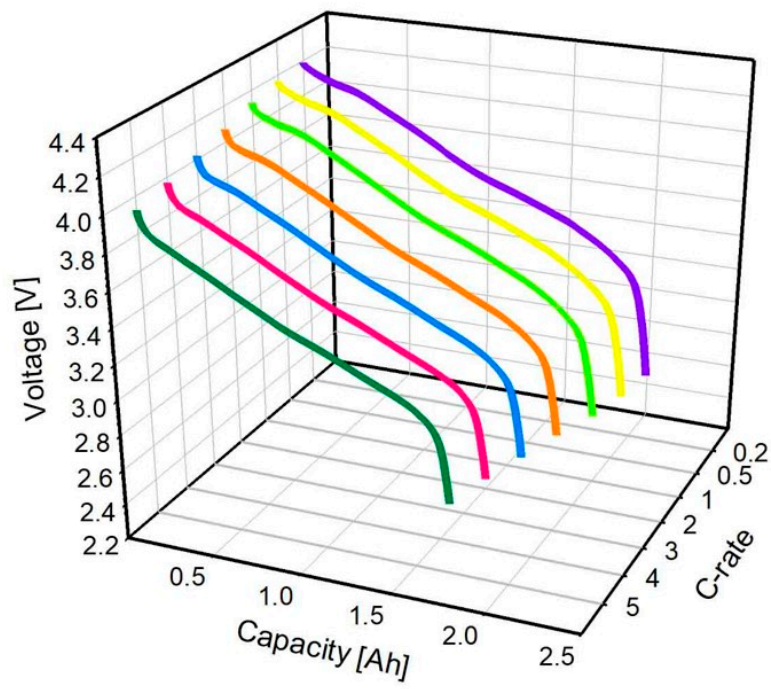
3.1.1. Battery Discharge Performance According to C-Rate Conditions

Capacity Loss

Figure 7a–d shows the capacity loss when discharging battery cells with different positive electrode materials at different discharge rates at 25 °C. At slow discharge rates of 0.2 and 0.5 C-rate, capacity reductions of 2.1% to 3.0% and 0.8% to 1.4% were observed in LFP and LMO compared to the existing capacity, and NCM 622 and NCM 811 were found to decrease by 4.1% to 5.4% and 2.7% to 4.5%, respectively. At the 1 C-rate, capacity decreases of 4.7% and 2.5% were observed in LFP and LMO and decreases of 7.6% and 7.1% in NCM 622 and NCM 811, respectively. It can be confirmed that the change in battery capacity was larger than the slow discharge rate. In the case of the 2–5 C-rates, which are fast discharge rates, capacity reductions of 7.7% to 15.8% and 5.1% to 9.8% were observed in LFP and LMO and 11.6% to 22.4% and 11.4% to 21.6% in NCM 622 and NCM 811, respectively, showing a larger range of capacity reduction.

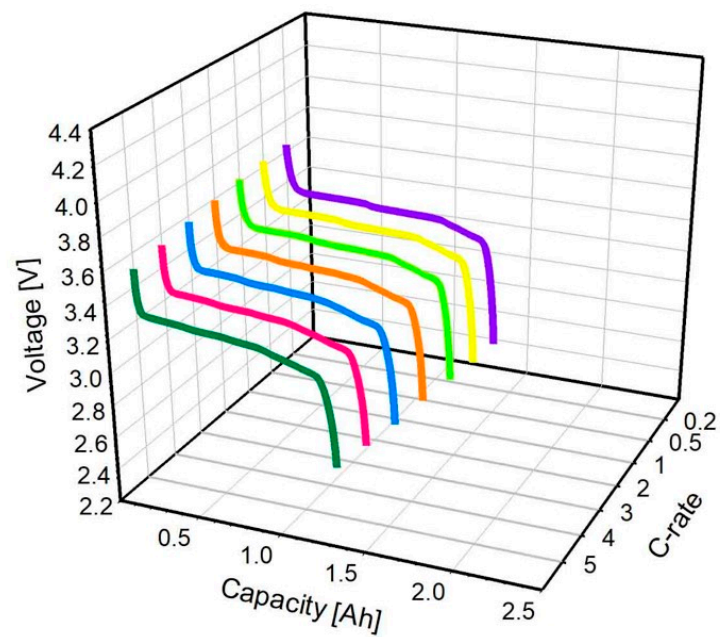


(a)

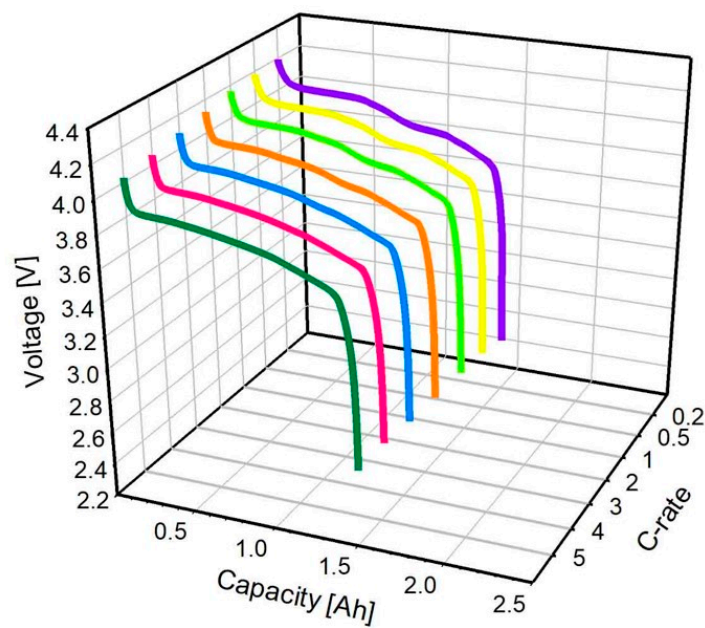


(b)

Figure 7. Cont.



(c)



(d)

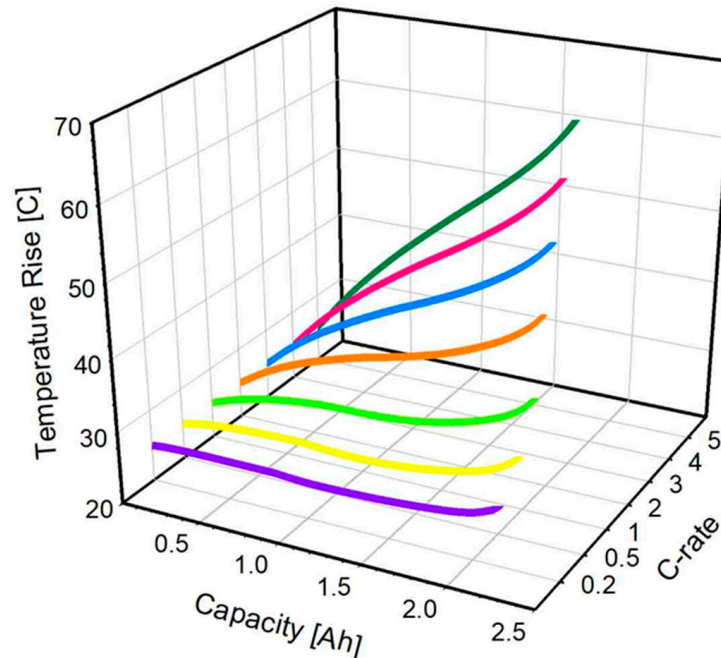
Figure 7. (a) Battery capacity loss for each positive electrode material when discharged at different C-rates under NCM 622. (b) Battery capacity loss for each positive electrode material when discharged at different C-rates under NCM 811. (c) Battery capacity loss for each positive electrode material when discharged at different C-rates under LFP. (d) Battery capacity loss for each positive electrode material when discharged at different C-rates under LMO.

As the discharge rate increased, the capacity loss of the battery also increased rapidly. The simulation showed that the change in the capacity of the battery according to the increase in discharge rate was larger in the NCM system than it was in the LFP and LMO systems. It is because NCM's layered structure characteristics had more intercalation space of Li-ion.

Temperature Change

Figure 8a–d shows the results of a temperature change when discharging battery cells with different positive electrode materials at different discharge rates at 25 °C. At slow discharge rates of 0.2 and 0.5 C-rates, compared to the initial temperature, the temperature increased by 0.8 °C and 1.5 °C and 1.0 °C and 1.9 °C in LFP and LMO and by 2.6 °C and 5.7 °C and 1.8 °C and 4.1 °C in NCM 622 and NCM 811, respectively, and the temperature change did not appear to be significant. At 1 C-rate, the LFP and LMO increased by 2.5 °C and 3.6 °C, and in the case of NCM 622 and NCM 811, the temperature increased by 10.3 °C and 8.0 °C, and it can be confirmed that the temperature increased more significantly than with the slow discharge rate. In the case of the 2–5 C-rates, which are fast discharge rates, temperature changes of 5.0 °C and 12.6 °C and 7.5 and 19.4 °C were observed in LFP and LMO, respectively. In NCM 622 and NCM8 11, the temperature increases were 18.5 °C and 36.8 °C and 15.6 °C and 33.3 °C, and the temperature change also increased as the discharge rate increased. The temperature change in the battery according to the discharge rate was probably due to the internal heat generation of the battery. [27] It was found that the Ni contents in NCM caused worse thermal stability due to their higher reactivity during discharging process while LMO and LFP with spinel and olivine structure can avoid excessive temperature rise.

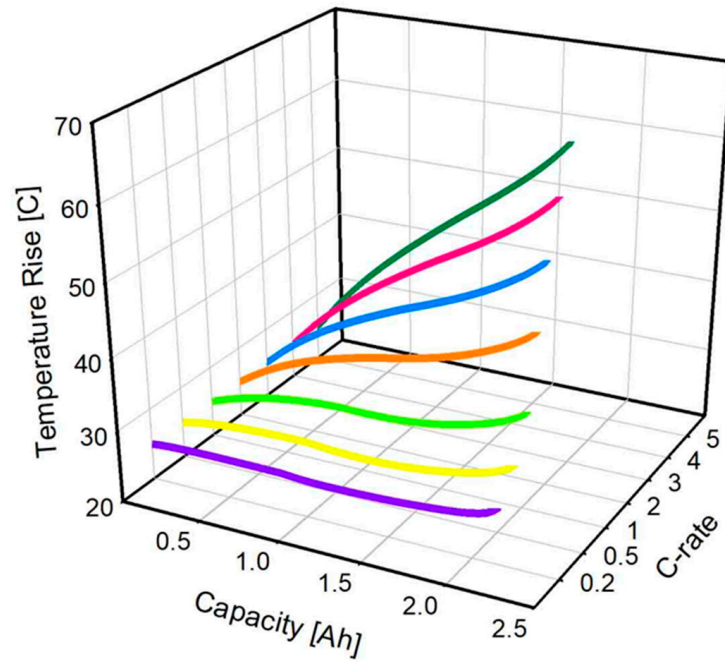
* NCM622 : Thermal model - Off



(a)

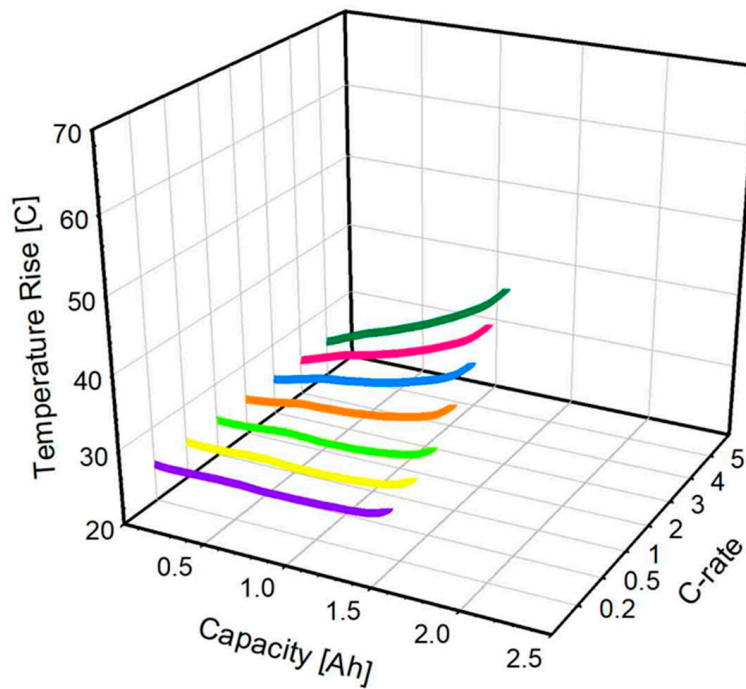
Figure 8. Cont.

* NCM811 : Thermal model - Off



(b)

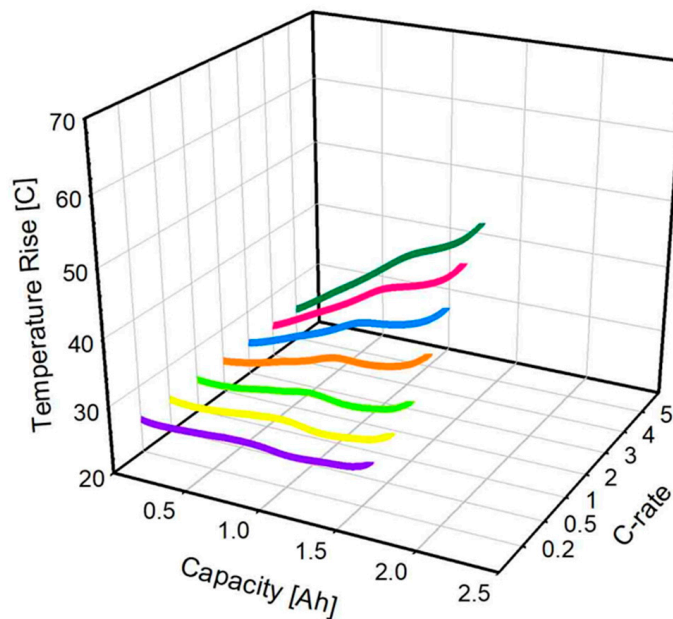
* LFP : Thermal model - Off



(c)

Figure 8. Cont.

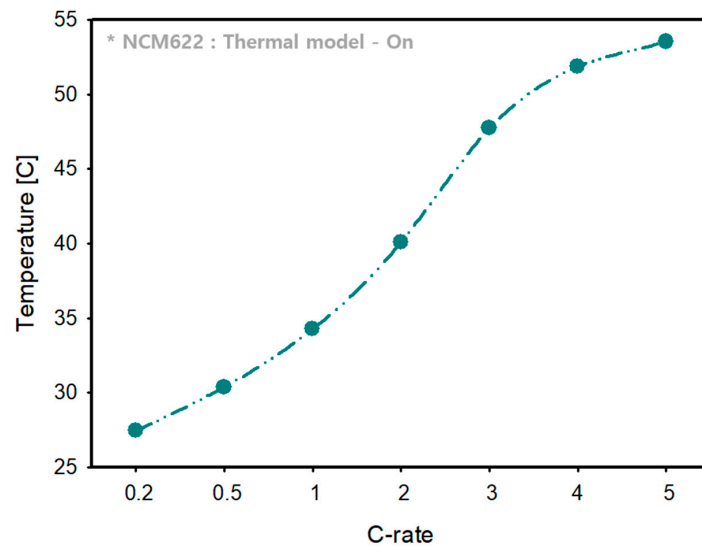
* LMO : Thermal model - Off



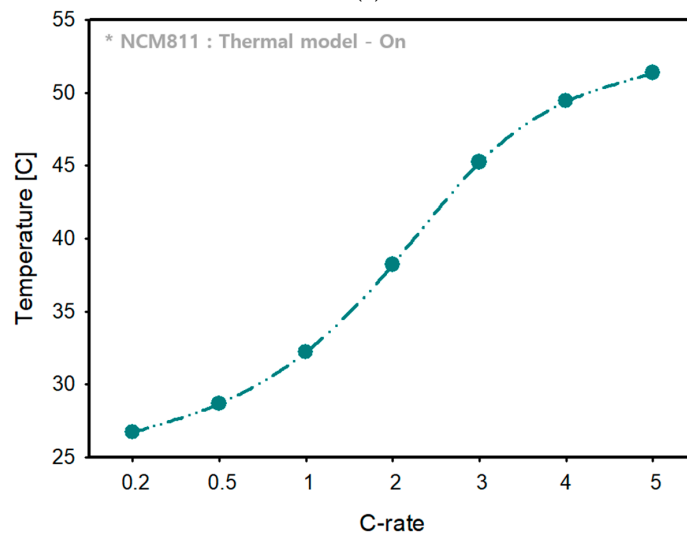
(d)

Figure 8. (a) Battery temperature change according to application of each positive electrode material when discharging at different C-rates without a thermal model under NCM 622. (b) Battery temperature change according to application of each positive electrode material when discharging at different C-rates without a thermal model under NCM 811. (c) Battery temperature change according to application of each positive electrode material when discharging at different C-rates without a thermal model under LFP. (d) Battery temperature change according to application of each positive electrode material when discharging at different C-rates without a thermal model under LMO.

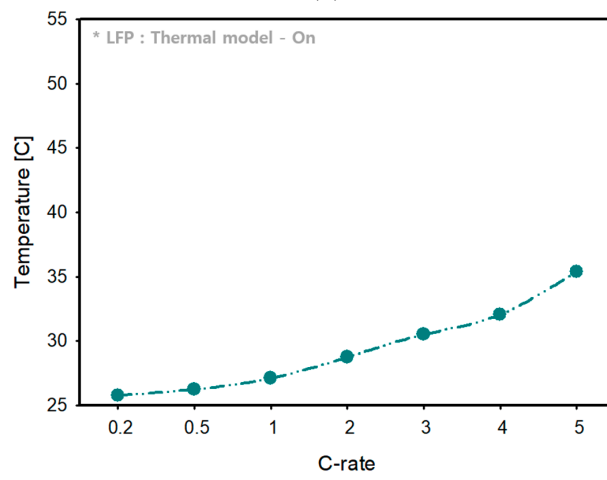
Figure 9a–d shows the temperature change in the battery when the thermal model was applied. As shown in Figures 8 and 9, it was confirmed that the temperature of the battery differed by a maximum of 8.3 °C, depending on whether a thermal model was applied at all discharge rates. The simulation showed that the increase in temperature with increasing discharge rate was less for the LFP than for the NCM system and LMO materials and, thus, LFP was an excellent material in terms of thermal properties with less intercalation of Li-ion on olivine structure and less reactivity during lithiation. When selecting materials in terms of safety, which is one of the characteristics required for EV batteries, it is considered that the safety of the battery can be secured by selecting an LFP material with excellent thermal properties.



(a)



(b)



(c)

Figure 9. Cont.

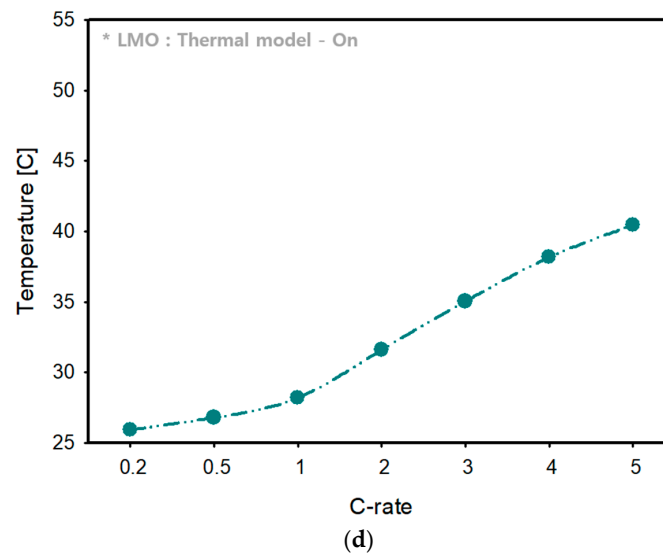
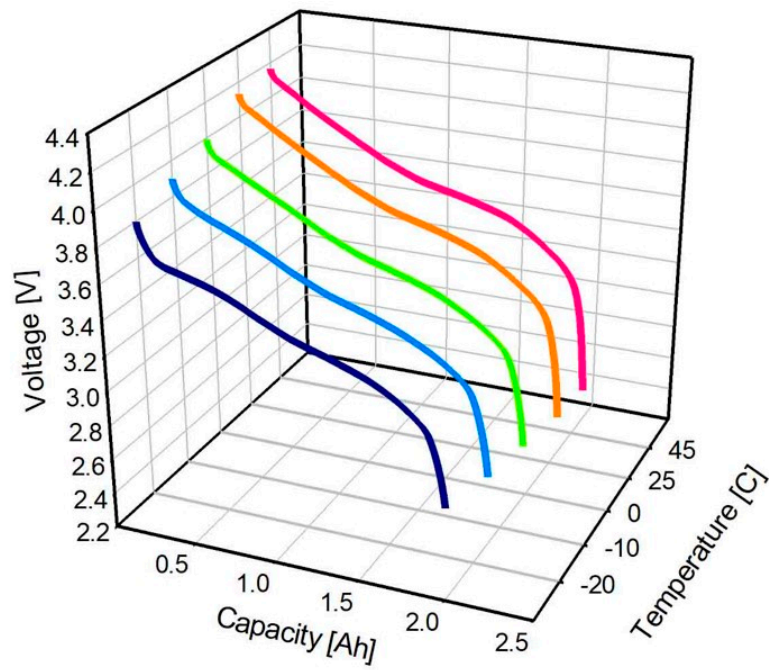


Figure 9. (a) Battery temperature change according to the application of each positive electrode material when discharging at different C-rates with a thermal model under NCM 622. (b) Battery temperature change according to the application of each positive electrode material when discharging at different C-rates with a thermal model under NCM 811. (c) Battery temperature change according to the application of each positive electrode material when discharging at different C-rates with a thermal model under LFP. (d) Battery temperature change according to the application of each positive electrode material when discharging at different C-rates with thermal model under LMO.

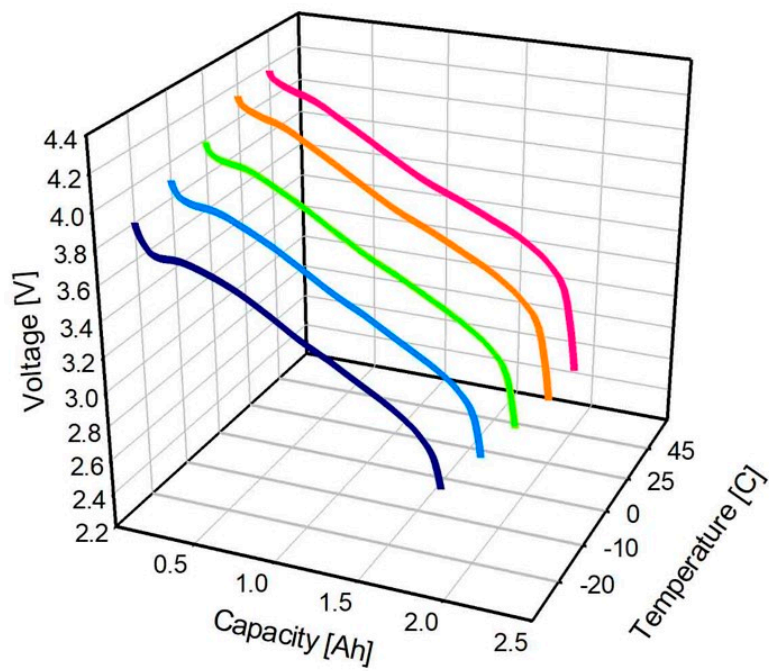
3.1.2. Battery Discharge Performance According to Temperature Conditions

Capacity Loss

Figure 10a–d shows the capacity loss when discharging battery cells of different positive electrode materials at a 1 C-rate under five different temperature conditions (-20 , -10 , 0 , 25 , and 45 °C). In the case of low temperatures, -20 , -10 , and 0 °C, in LFP and LMO, the capacity decreased by 29.1%, 18.8%, and 11.8% and 21.2%, 13.8%, and 8.5% compared to the existing capacity. For the room temperature, 25 °C, and high temperature, 45 °C, capacity reductions of 4.7% and 2.9% and 2.5% and 1.2% were observed in LFP and LMO compared to the existing capacity, and capacity reductions of 7.6% and 6.7% and 7.1% and 6.2% were found in NCM 622 and NCM 811. Thus, it can be confirmed that the capacity reductions at these temperatures were less than those at low temperatures. In a low-temperature environment, the internal chemical reaction rate of the battery slows down, resulting in a decrease in operating voltage and capacity, which leads to a decrease in the battery performance. [28] On the other hand, as the temperature increases, the chemical reaction becomes more active and the capacity decrease is smaller. The simulation results indicated that the LFP and LMO materials showed less capacity reduction than did the NCM-based materials at room and high temperatures. However, the capacity decreased rapidly in low temperatures. It was confirmed that the NCM material was relatively more stable in all temperature regions.

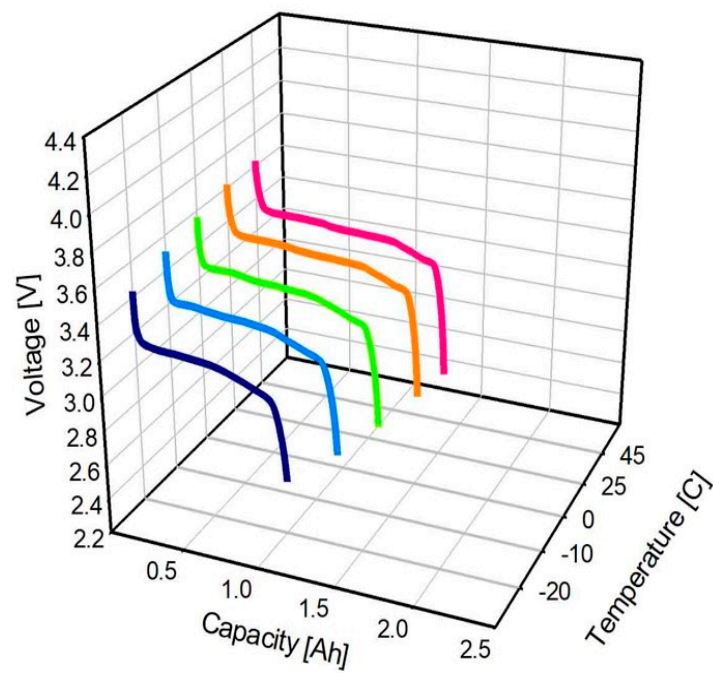


(a)

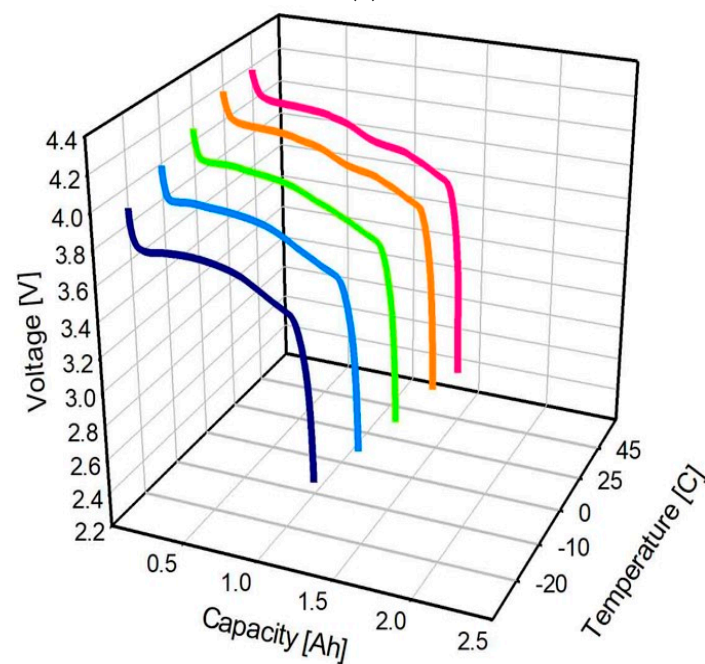


(b)

Figure 10. Cont.



(c)



(d)

Figure 10. (a) Battery capacity loss when discharged at 1 C-rate at -20 , -10 , 0 , 25 , and 45 °C under NCM 622. (b) Battery capacity loss when discharged at 1 C-rate at -20 , -10 , 0 , 25 , and 45 °C under NCM 811. (c) Battery capacity loss when discharged at 1 C-rate at -20 , -10 , 0 , 25 , and 45 °C under LFP. (d) Battery capacity loss when discharged at 1C-rate at -20 , -10 , 0 , 25 , and 45 °C under LMO.

Temperature Change

Figure 11a–d shows the temperature changes when discharging battery cells of different positive electrode materials at 1 C-rate under five different temperature conditions. In the case of low temperatures, -20 , -10 , and 0 °C, in LFP and LMO, the temperatures increased by 8.1 °C, 6.0 °C,

and 4.4 °C and 11.9 °C, 8.9 °C, and 6.6 °C, and the temperatures increased by 22.4 °C, 18.7 °C, and 15.7 °C and 20.7 °C, 16.6 °C, and 13.4 °C in NCM 622 and NCM 811. At room temperature (25 °C) and high temperature (45 °C), the temperatures increased by 2.5 °C and 2.2 °C and 3.6 °C and 2.9 °C in LFP and LMO, and the temperatures increased by 10.3 °C and 7.6 °C and 8.0 °C and 5.3 °C in NCM 622 and NCM 811, and it can be confirmed that the temperature changed less at low temperatures. In the case of the NCM material, a small decrease in capacity occurred because the temperature rise during the discharge in the low-temperature region was larger than that in the LFP and LMO materials. However, in the LFP and LMO materials, the capacity decrease was large because the temperature rise was small during the discharge in the low-temperature region. Thus, it seems that the more active the chemical reaction was at low temperatures, the more the temperatures rose and the less the voltage dropped; therefore, the battery capacity did not decrease as much.

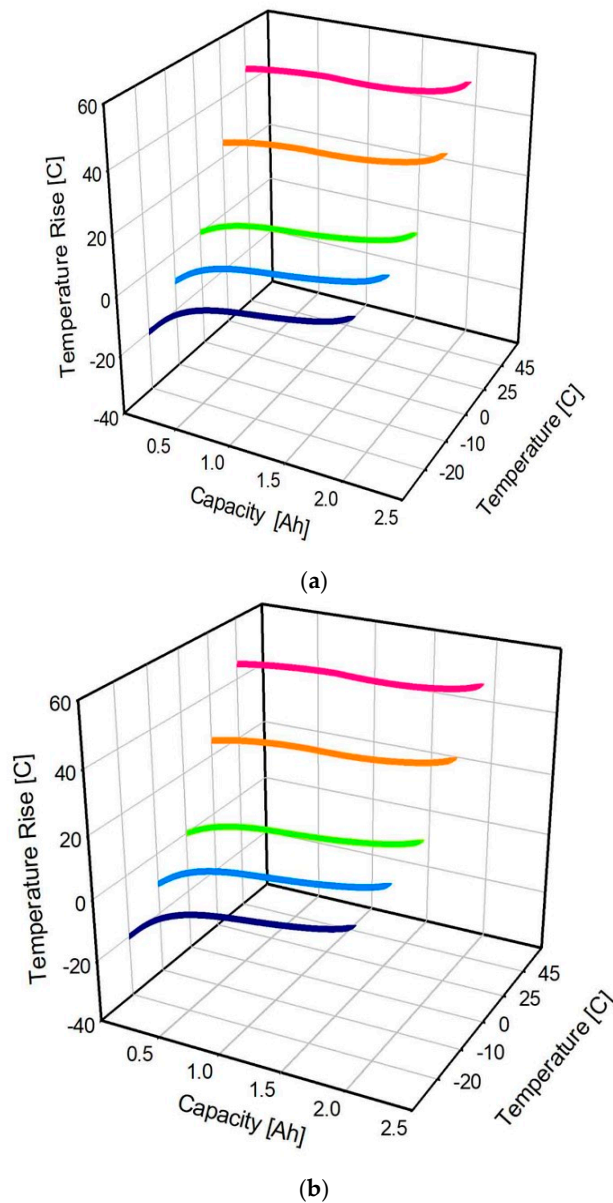
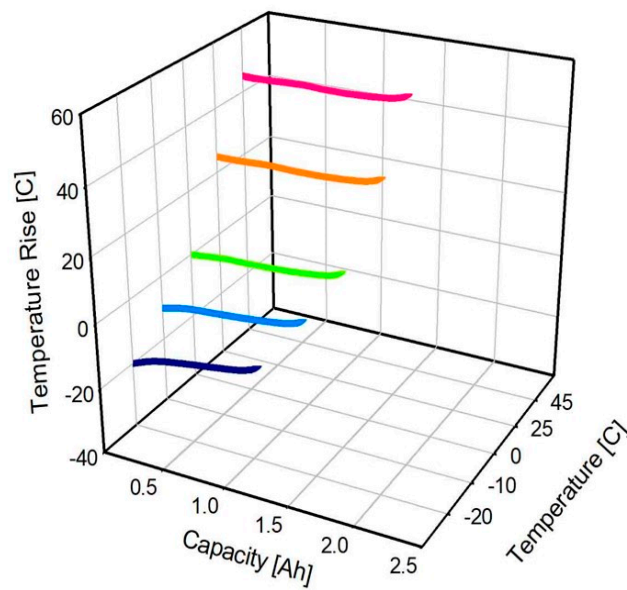
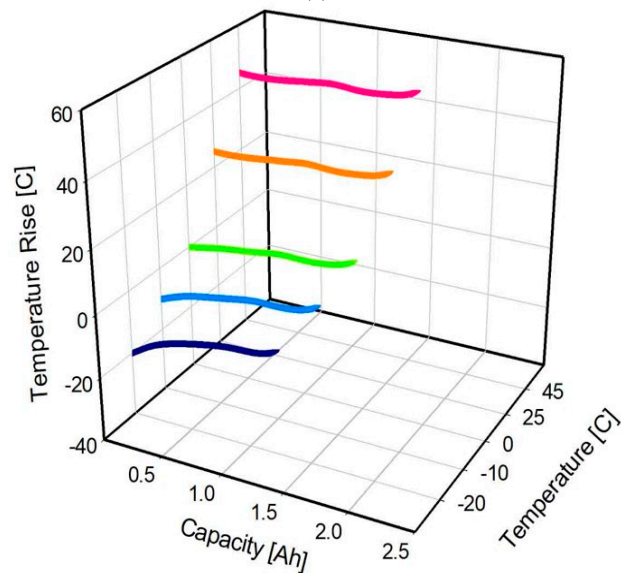


Figure 11. Cont.



(c)



(d)

Figure 11. (a) Battery temperature change when discharged at 1 C-rate at -20 , -10 , 0 , 25 , and 45 °C under NCM 622. (b) Battery temperature change when discharged at 1 C-rate at -20 , -10 , 0 , 25 , and 45 °C under NCM 811. (c) Battery temperature change when discharged at 1 C-rate at -20 , -10 , 0 , 25 , and 45 °C under LFP. (d) Battery temperature change when discharged at 1 C-rate at -20 , -10 , 0 , 25 , and 45 °C under LMO.

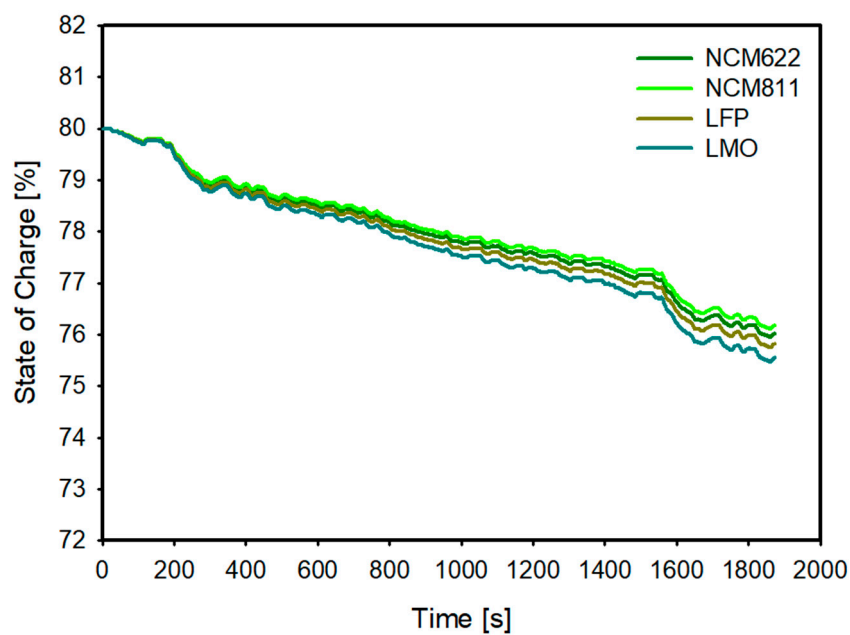
3.2. Analysis of EV Characteristics According to Battery Pack by Type of Positive Electrode Active Material

3.2.1. Comparison Analysis of Characteristics of the Battery Model According to the Application of the Driving Cycle

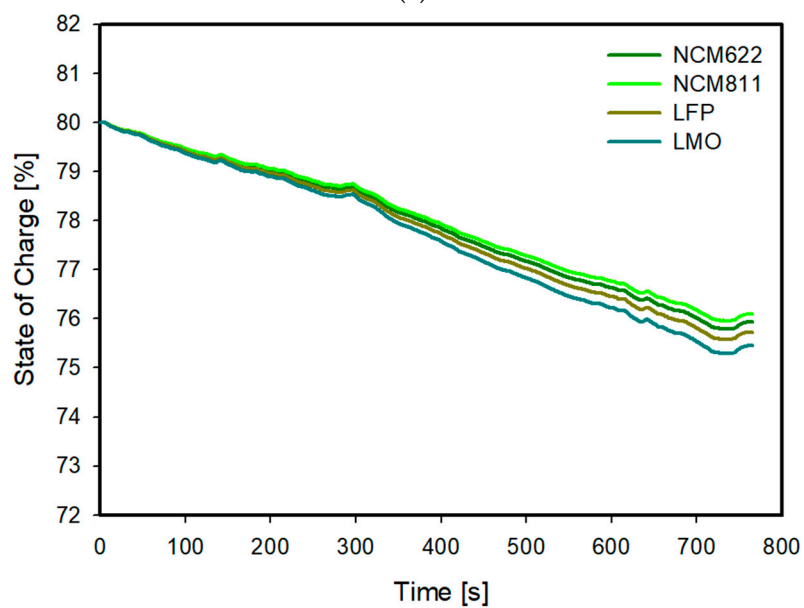
SOC

Figure 12a–d shows the changes in battery SOC according to four different driving cycles for batteries with different positive electrode materials. Four types of positive electrode materials were applied in each driving cycle. In the city center driving cycle FTP-75 compared to the initial SOC (80%),

for NCM622 and NCM811, SOC reductions of 4.0% and 2.5% were observed, and the SOC in LFP and LMO decreased by 4.2% and 4.5%, respectively. In the HWFET, which is a high-speed driving cycle, and US06 driving cycles, SOC reductions of 4.1% and 3.9% were observed in NCM 622 and NCM 811, and in LFP and LMO, the reductions were 4.3% and 4.6%, respectively. The reduction range was similar to that in the FTP-75 driving cycle. In the WLTC cycle, which is divided into four speeds, from low to ultra-high, SOC reductions of 6.1% and 5.9% were observed in NCM6 22 and NCM 811. In LFP and LMO, the reductions were 6.4% and 6.8%, respectively, showing a larger SOC reduction compared to the other three driving cycles. This cycle had a larger speed change than the other cycles due to cycle characteristics, and, in addition, the rapid speed change, high maximum speed, and mileage had an effect on the SOC reduction.

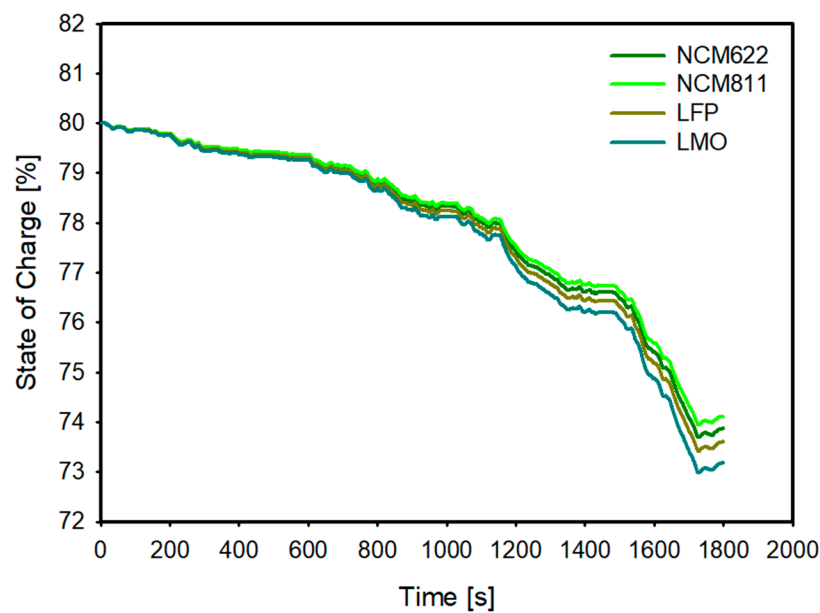


(a)

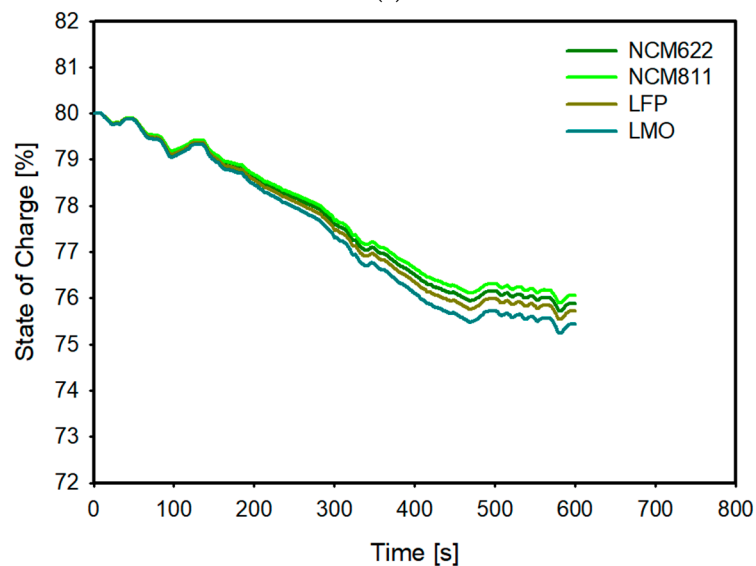


(b)

Figure 12. Cont.



(c)



(d)

Figure 12. (a) Comparison of changes in battery SOC under FTP-75. (b) Comparison of changes in battery SOC under HWFET. (c) Comparison of changes in battery SOC under WLTC. (d) Comparison of changes in battery SOC under US06.

Battery Weight

To improve the fuel efficiency of EVs, it is essential to increase the capacity and weight of the battery pack, which is a key component of EVs. Increasing both the capacity and energy density of the battery can effectively improve the efficiency of the EV; therefore, we compared the weights of the battery pack. Figure 13 shows the comparison of the battery pack weights for the EVs according to the application of the positive electrode material. For the same construction with a 55-kWh battery for the target EV and with NCM 622 and NCM 811, the weights were found to be 293.4 and 299.2 kg, and the weights were 450.9 and 381.1 kg for LFP and LMO. As a result of comparing the battery packs, to which each of the four positive electrode materials were applied, those using NCM 622 and NCM 811 were found to be 157.5 and 87.8 kg and 151.7 and 82.0 kg lighter than those using LFP and LMO materials, respectively. Because of the advantage that NCM-based positive electrode materials have

with a relatively higher energy density than LFP and LMO, they can build the same capacity with a lighter weight; therefore, when selecting materials from the viewpoint of high-capacity and lightweight characteristics, the NCM system is more suitable for EV applications.

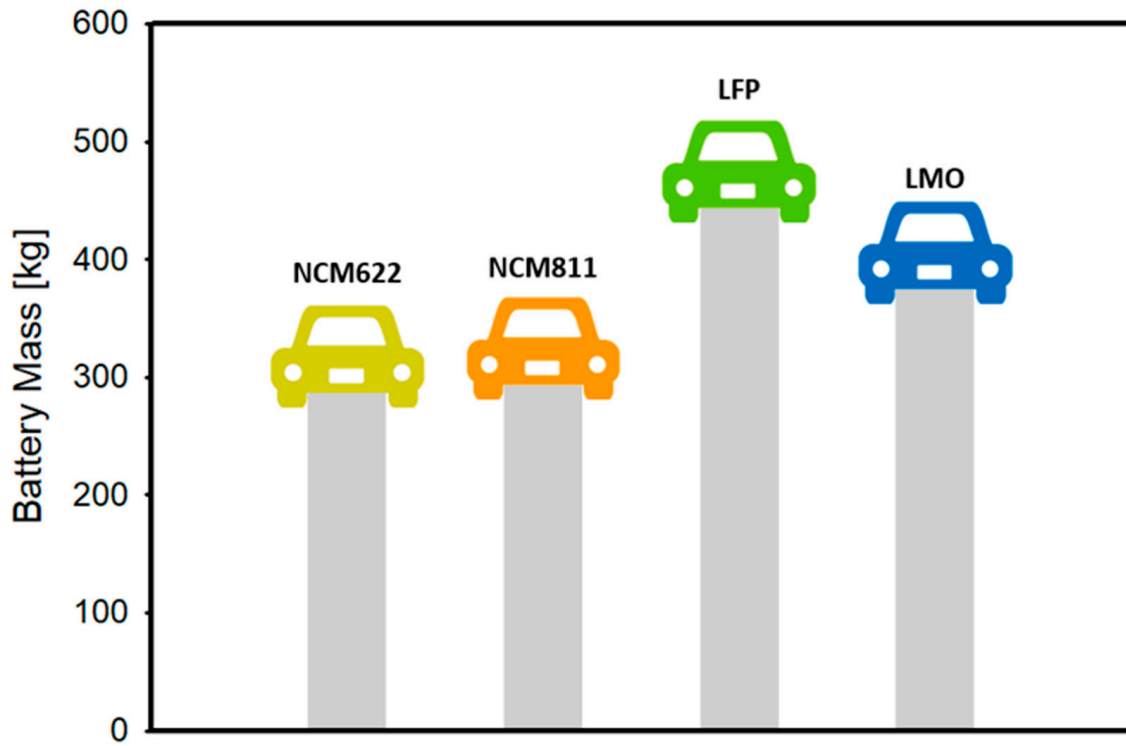


Figure 13. Comparison of weight according to the application of different positive electrode materials for the battery pack mounted in the EV.

Capacity Loss

Figure 14a–d shows the changes in the EV battery capacities of different positive electrode materials according to the application of four driving cycles. As a result of applying each of the four positive electrode materials in each driving cycle, in the FTP-75 cycle, capacity reductions of 10.2 Ah and 10.1 Ah were observed for NCM 622 and NCM 811 compared to the existing capacity, and the capacities for LFP and LMO decreased by 11.0 Ah and 10.9 Ah. In the HWFET and US06 cycles, capacity reductions of 7.0 Ah and 6.9 Ah and 9.5 Ah and 9.4 Ah were observed for NCM 622 and NCM 811, and for LFP and LMO, the capacities decreased by 7.6 Ah and 10.3 Ah and 7.5 Ah and 10.2 Ah. Of the four cycles, the HWFET with the smallest rate change showed a small capacity reduction range. In the WLTC cycle, capacity changes of 13.3 Ah and 13.2 Ah were observed for NCM 622 and NCM 811, and the capacity changes for LFP and LMO were 14.4 Ah and 14.2 Ah, respectively, which significantly reduced the capacity compared to the other three driving cycles. Compared to other materials, the capacity reduction of the NCM 811 material was the lowest. On the other hand, LFP showed the greatest reduction in capacity. These results suggest that the characteristics of each material are well reflected according to the metal composition ratio of the Li [Ni, Co, Mn] O₂ ternary system.

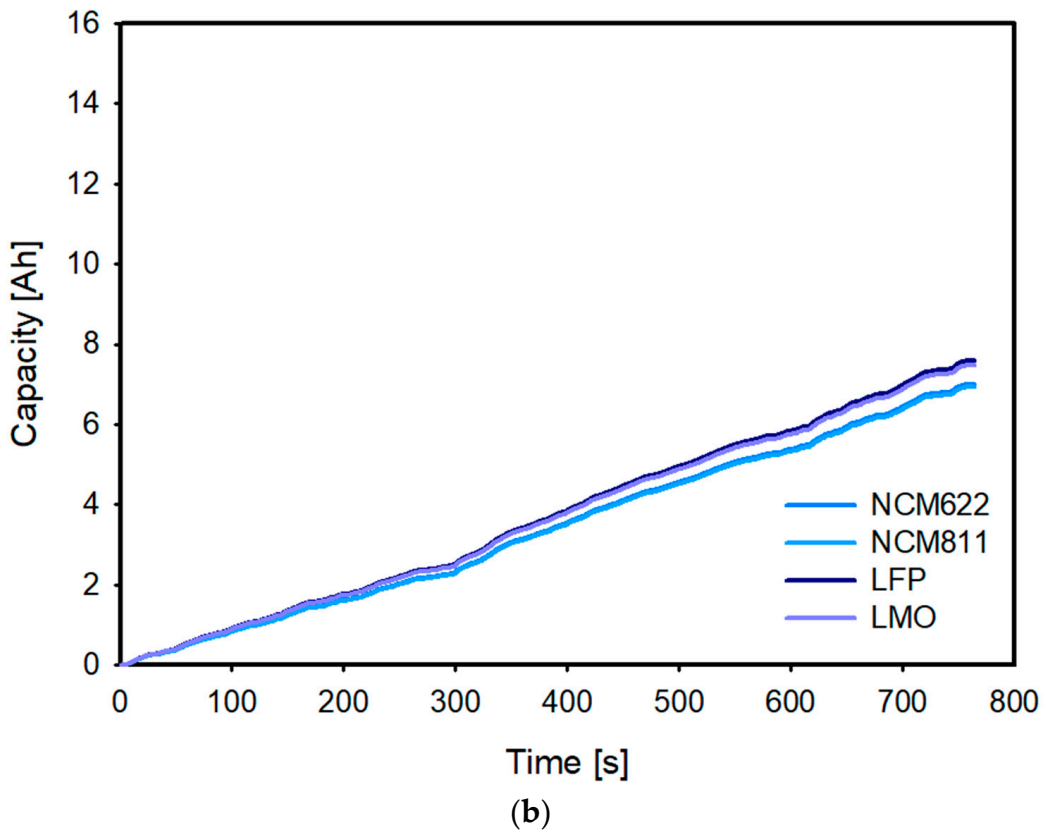
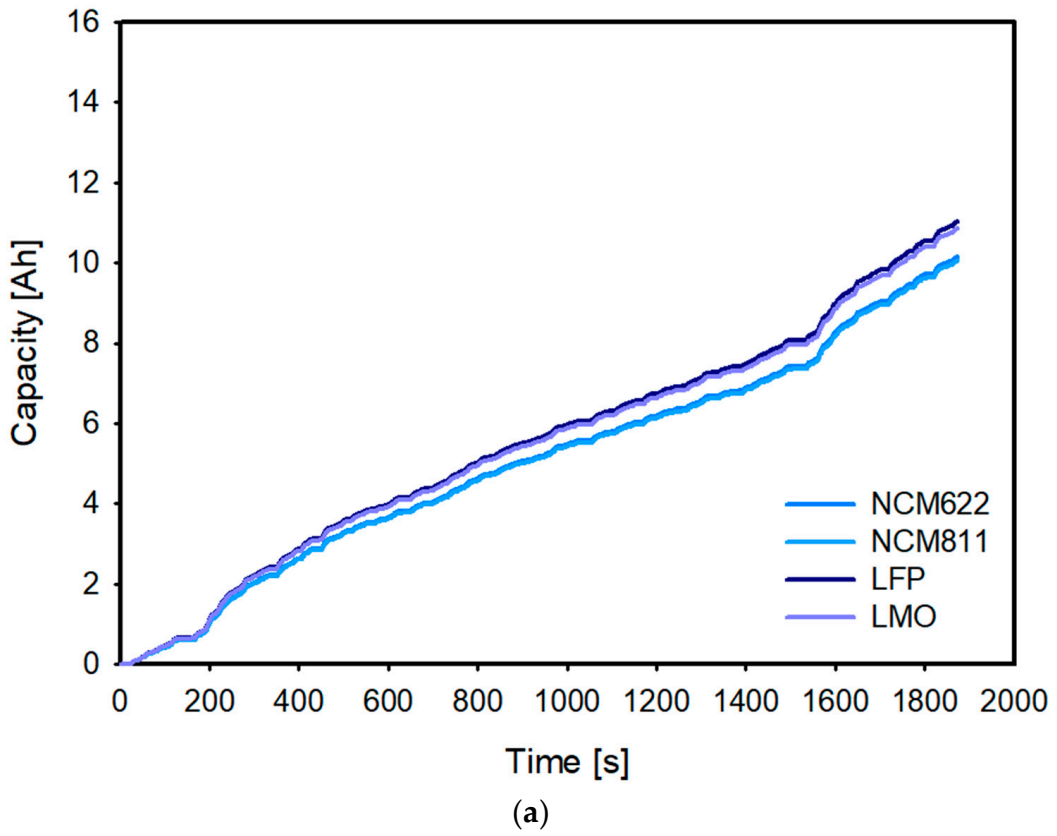
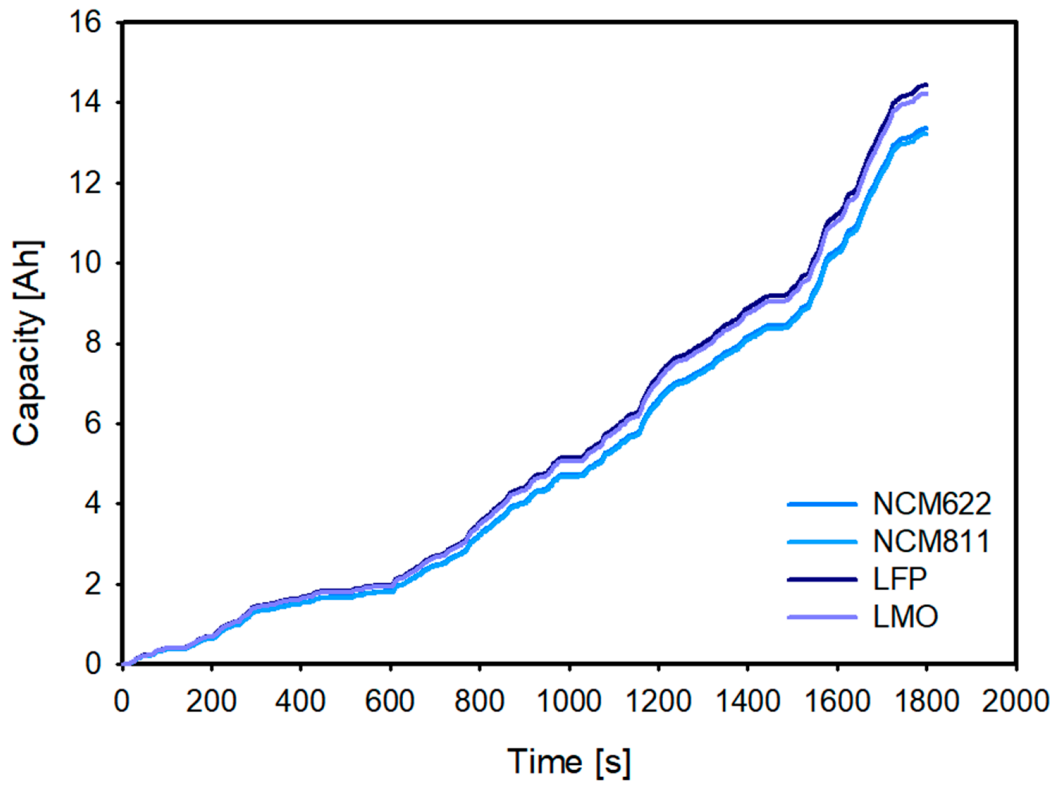
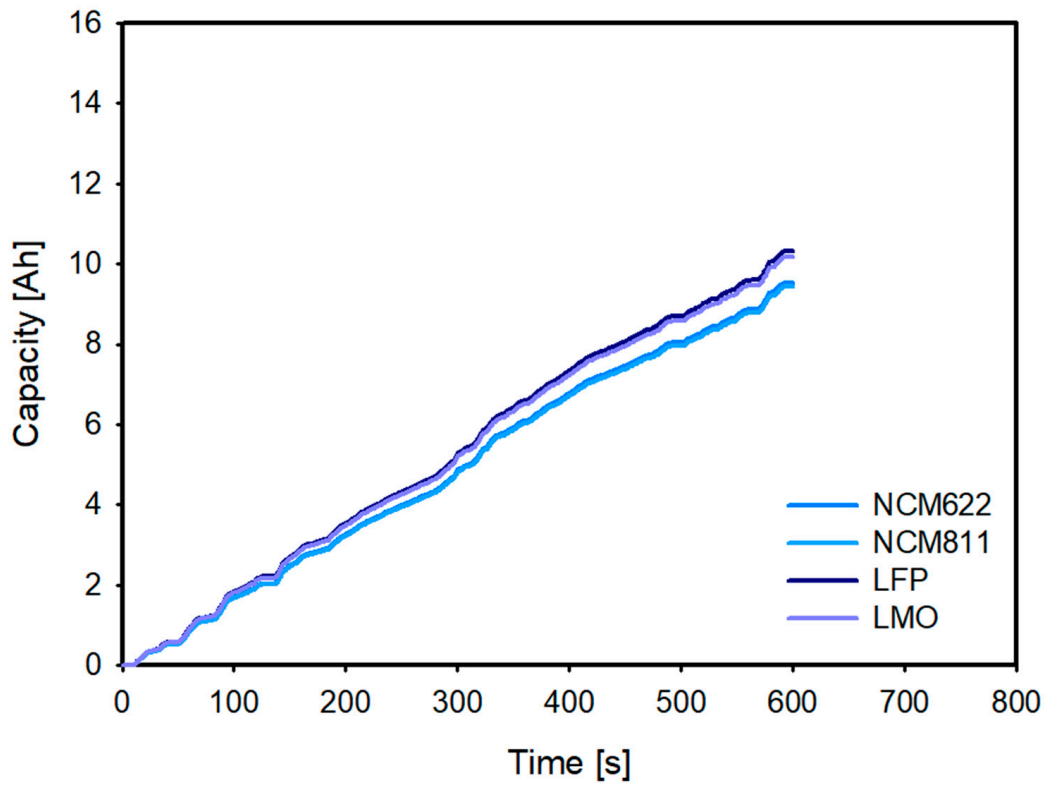


Figure 14. Cont.



(c)



(d)

Figure 14. (a) Comparison of battery capacity loss under FTP-75. (b) Comparison of battery capacity loss under HWFET. (c) Comparison of battery capacity loss under WLTC. (d) Comparison of battery capacity loss under US06.

3.3. Battery Cell Model: Comparative Analysis of Trends through Experimental and Simulation Results

3.3.1. Capacity Loss

Figure 15 shows the comparison of the battery capacity losses in the simulation and experiment when discharging battery cells of NCM positive electrode material at different discharge rates at 25 °C. To verify the validity of the simulation results, using 18650 cylindrical batteries with NCM material, charge and discharge tests were performed at speeds of 0.2, 0.5, 1, and 2 C-rate, and a comparative analysis of the changes in battery capacity according to the discharge speed was conducted. When comparing the simulation and experimental results, the results of the simulation of the battery cell, to which NCM 622 was applied, were used. A comparison of the battery capacity loss according to different discharge rates indicated that at 0.2 and 0.5 C-rate, 4.0% and 4.7% capacity reductions were observed, and at 1 and 2 C-rate, the reductions were 6.3% and 9.6%, respectively, which was a larger capacity reduction range. Through the experiment and simulation results, it was confirmed that the tendencies for the battery capacity loss to increase as the discharge rate increased were the same. In addition, the values of the capacity reduction obtained through GT-AutoLion appeared larger than those in the experiment, and the error between the experimental and simulation values increased as the discharge rate increased; however, the error rate was within 10%. It seems that the main cause of error between experiment and simulation results was unknown material properties. It was already mentioned that the present study aimed for identification of feasibility over accurate calibration by comparing the minimum available experimental data and raw simulation data without parameter tune. If calibration processes were performed in terms of general electrochemical parameter for LIB calibration such as N/P ratio, capacity loading and error bound could be significantly reduced. Even though there was no calibration, an error within 10% is judged as good model accuracy.

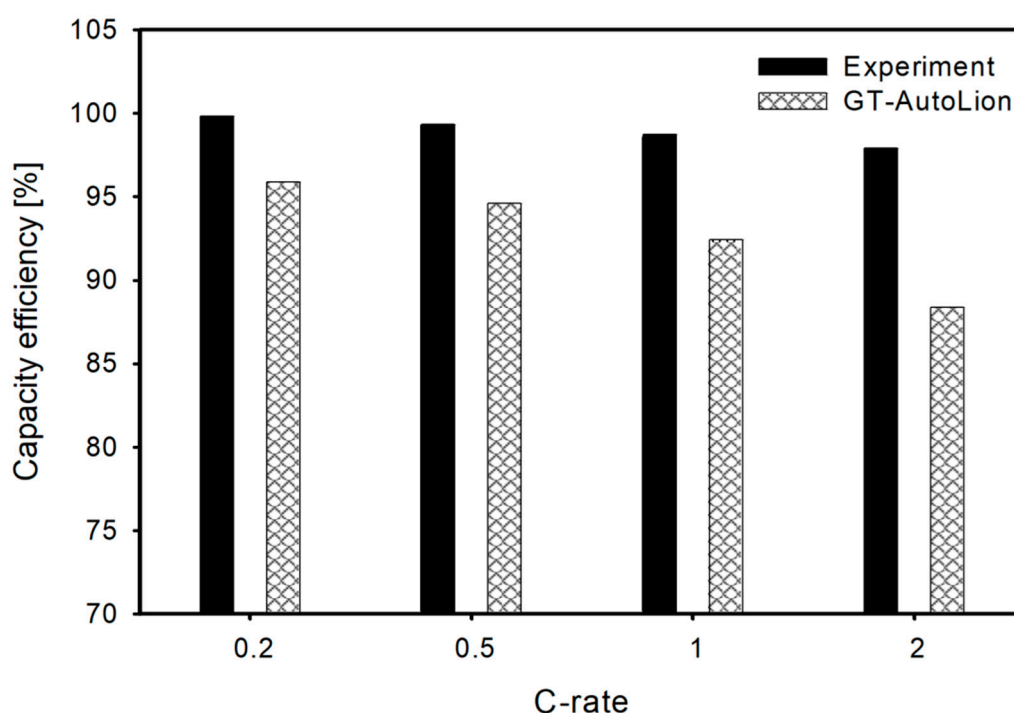


Figure 15. Comparison of the capacity loss for an 18650 cylindrical battery with NCM material according to different C-rates.

3.3.2. Temperature Change

Figure 16 shows a comparison of the battery temperature changes in the simulations and experiments when discharging battery cells of NCM positive electrode material at different discharge

rates under a 25 °C temperature. A total of three results was compared: simulations with and without a thermal model and the experiment. First, comparing the simulation and experimental results with an applied thermal model, at 0.2 and 0.5 C-rates, differences of 1.7 °C and 3.9 °C were observed compared to the initial temperature, and at 1 and 2 C-rates, differences of 6.3 °C and 8.2 °C appeared. Comparing the simulation and experimental results with no applied thermal model, at 0.2 and 0.5 C-rates, differences of 1.8 °C and 4.3 °C were observed compared to the initial temperature, and at 1 and 2 C-rates, the temperature changes were 7.4 °C and 11.6 °C and appeared larger than those at the slow discharge rate (0.2, 0.5 C-rates). This comparison indicated that as the discharge rate increased, the tendency for the temperature of the battery to increase was the same for both the experiment and the simulation, and it can be seen that the result of the simulation was more excessive than that of the experiment. In general, the LIB had a temperature gradient due to internal heat generation during charging and discharging. According to the research results of Zhang et al., the internal temperature of the battery during charging and discharging appears higher than the surface temperature, and as the discharge rate increases, the temperature gradient also increases, owing to more heat generation. [29]. It seems that the main cause of error between experiment and simulation results was fixed heat transfer coefficient approach. As C-rate increases with relatively rapid discharge, Q_{gen} from Equation (6) was changed, resulting in more temperature difference between inside and outer space of battery. Therefore, convection heat transfer coefficient, h , has to be validated under each C-rate condition. It was judged as an error that occurred because variable tuning was not performed in this study. If heat transfer coefficient is handled for calibration as further study, prediction accuracy will be remarkably enhanced.

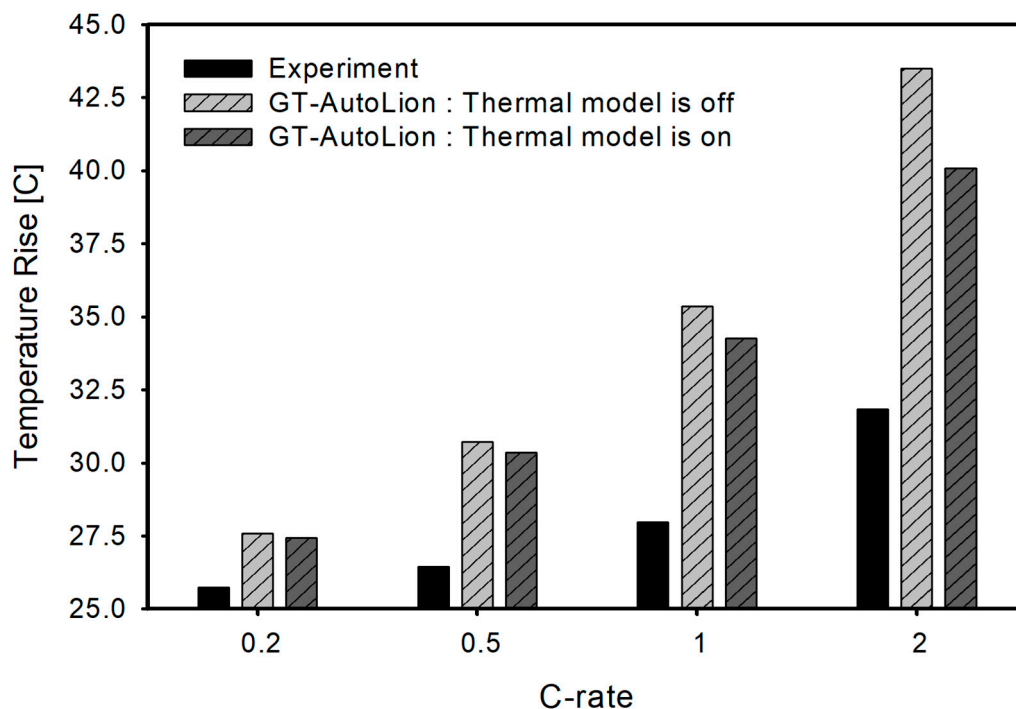


Figure 16. Comparison of the temperature change for the 18650 cylindrical battery with NCM material according to different C-rates.

4. Conclusions and Future Work

In this study, LIB was modeled from a cylindrical battery cell to an EV system using GT-AutoLion based on a thermally coupled electrochemical model. The main objective of our overall study was to provide a reverse calibration method and fast design processes of LIB, although there was a lack of model calibration processes. As the first step, the present study aimed for identification of feasibility

over accurate calibration by comparing the minimum available experimental data and raw simulation data without parameter tune. Based on the results, the following conclusions can be drawn.

- As the C-rate increased, the battery capacity loss and temperature increased, and it was confirmed that the NCM system was more affected by the C-rate than were LFP and LMO. If the safety of an EV is considered first, a higher safety can be secured when LFP, a positive electrode material with excellent thermal characteristics, is applied to a battery, rather than NCM. At room temperature and higher temperatures, LFP and LMO materials showed less capacity loss than did NCM. On the other hand, LFP and LMO materials at low temperatures showed a sharp loss in capacity. This is because NCM is relatively more active in chemical reactions than are LFP and LMO, even at low temperatures. Therefore, it was confirmed that NCM is relatively more stable than LFP and LMO in all temperature regions. Through the cell simulation, as for the state of charge, NCM was excellent, while LFP and LMO were excellent for thermal stability.
- These trends were similar in battery pack and driving cycle transient analysis. However, when considering the weight of the battery in the EV level, NCM is competitive, which is also the reason why NCM is widely used nowadays. Nevertheless, since thermal stability is becoming increasingly important to battery sustainability, hybrid cathode material technology that combines the advantages of each material is needed.
- It can be seen that the battery and EV characteristics with each positive electrode active material can follow the trend without variable tuning. Based on this, complementary studies will be conducted in the future. A cell-by-cell calibration will be performed to access the top-down design. At this time, optimization will be performed by deriving tuning variables that affect thermal stability, SOC maintenance, and vehicle weight.

Author Contributions: Conceptualization, methodology, validation, formal analysis, investigation and writing—original draft preparation, H.C.; Experimental support, N.-g.L.; Supervision of experiment, S.J.L.; Supervision, writing—review and editing, J.P. All authors have read and agreed to the published version of the manuscript.

Funding: This work was funded by Chosun University (No. K207469003-1, Conjugate heat transfer analysis for optimization of EV battery cooling performance).

Acknowledgments: This work was supported by Chosun University (No. K207469003-1, Conjugate heat transfer analysis for optimization of EV battery cooling performance).

Conflicts of Interest: The authors declare no conflict of interest.

References

1. Jiang, L.; Wang, Q.; Sun, J. Electrochemical performance and thermal stability analysis of $\text{LiNi}_x\text{Co}_y\text{Mn}_z\text{O}_2$ cathode based on a composite safety electrolyte. *J. Hazard. Mater.* **2018**, *351*, 260–269. [[CrossRef](#)] [[PubMed](#)]
2. Zybert, M.; Ronduda, H.; Szczesna, A.; Trzeciak, T.; Ostrowski, A.; Zero, E.; Wiczczyk, W.; Rarog-Pilecka, W.; Marcinek, M. Different strategies of introduction of lithium ions into nickel-manganese-cobalt carbonate resulting in $\text{LiNi}_{0.6}\text{Mn}_{0.2}\text{Co}_{0.2}\text{O}_2$ (NMC622) cathode material for Li-ion batteries. *Solid State Ion.* **2020**, *348*, 115273. [[CrossRef](#)]
3. Ma, Z.; Shao, G.; Wang, G.; Zhang, Y.; Du, J. Effects of Nb-doped on the structure and electrochemical performance of LiFePO_4/C composites. *J. Solid State Chem.* **2014**, *210*, 232–237. [[CrossRef](#)]
4. Liu, Q.; Wang, S.; Tan, H.; Yang, Z.; Zeng, J. Preparation and Doping Mode of Doped LiMn_2O_4 for Li-Ion Batteries. *Energies* **2013**, *6*, 1718–1730. [[CrossRef](#)]
5. Ge, T.; Guo, Z.; Wu, M.; Sun, R.; Li, W.; Yang, G. Preparation and characterization of spinel-layered mixed structural $0.2\text{LiNi}_{0.5}\text{Mn}_{1.5}\text{O}_4 \cdot 0.8\text{Li}[\text{Li}_{0.2}\text{Ni}_{0.2}\text{Mn}_{0.6}]\text{O}_2$ as cathode materials for lithium-ion batteries. *J. Alloys Compd.* **2019**, *801*, 254–261. [[CrossRef](#)]
6. Ku, L.; Cai, Y.; Ma, Y.; Zheng, H.; Liu, P.; Qiao, Z.; Xie, Q. Enhanced electrochemical performances of layered-spinel heterostructured lithium-rich $\text{Li}_{1.2}\text{Ni}_{0.13}\text{Co}_{0.13}\text{Mn}_{0.54}\text{O}_2$ cathode materials. *Chem. Eng. J.* **2019**, *370*, 499–507. [[CrossRef](#)]
7. Zhao, Y.; Stein, P.; Bai, Y.; Al-Siraj, M.; Yang, Y.; Xu, B.X. A review on modeling of electro-chemo-mechanics in lithium-ion batteries. *J. Power Sources* **2019**, *413*, 259–283. [[CrossRef](#)]

8. Ning, F.; Li, S.; Xu, B.; Ouyang, C. Strain tuned Li diffusion in LiCoO₂ material for Li ion batteries: A first principles study. *Solid State Ion.* **2014**, *263*, 46–48. [[CrossRef](#)]
9. Stein, P.; Xu, B. 3D Isogeometric Analysis of intercalation-induced stresses in Li-ion battery electrode particles. *Comput. Methods Appl. Mech. Eng.* **2014**, *268*, 225–244. [[CrossRef](#)]
10. Tealdi, C.; Heath, J.; Islam, M.S. Feeling the strain: Enhancing ionic transport in olivine phosphate cathodes for Li- and Na-ion batteries through strain effects. *J. Mater. Chem. A* **2016**, *4*, 6998–7004. [[CrossRef](#)]
11. Salvadori, A.; Mcmeeking, R.; Grazioli, D.; Magri, M. A coupled model of transport-reaction-mechanics with trapping. Part I- small strain analysis. *J. Mech. Phys. Solids* **2018**, *114*, 1–30. [[CrossRef](#)]
12. Jia, Z.; Li, T. Stress-modulated driving force for lithiation reaction in hollow nano-anodes. *J. Power Sources* **2015**, *275*, 866–876. [[CrossRef](#)]
13. Ji, L.; Guo, Z.; Wu, Y. Computational and Experimental Observation of Li-Ion Concentration Distribution and Diffusion-Induced Stress in Porous Battery Electrodes. *Energy Technol.* **2017**, *5*, 1702–1711. [[CrossRef](#)]
14. Chen, C.H.; Liu, J.; Amine, K. Symmetric cell approach and impedance spectroscopy of high power lithium-ion batteries. *J. Power Sources* **2001**, *96*, 321–328. [[CrossRef](#)]
15. Park, J.; Lu, W.; Sastry, A.M. Numerical Simulation of Stress Evolution in Lithium Manganese Dioxide Particles due to Coupled Phase Transition and Intercalation. *J. Electrochem. Soc.* **2011**, *158*, A201–A206. [[CrossRef](#)]
16. Suthar, B.; Northrop, P.W.C.; Braatz, R.D.; Subramanian, V.R. Optimal Charging Profiles with Minimal Intercalation-Induced Stresses for Lithium-Ion Batteries Using Reformulated Pseudo 2-Dimensional Models. *J. Electrochem. Soc.* **2014**, *161*, F3144–F3155. [[CrossRef](#)]
17. Suthar, B.; Northrop, P.W.C.; Rife, D.; Subramanian, V.R. Effect of Porosity, Thickness and Tortuosity on Capacity Fade of Anode. *J. Electrochem. Soc.* **2015**, *162*, A1708–A1717. [[CrossRef](#)]
18. Dai, Y.; Cai, L.; White, R.E. Simulation and analysis of stress in a Li-ion battery with a blended LiMn₂O₄ and LiNi_{0.8}Co_{0.15}Al_{0.05}O₂ cathode. *J. Power Sources* **2014**, *247*, 365–376. [[CrossRef](#)]
19. Zhao, L.; Zhu, M.T.; Xu, X.M.; Gao, J.K. Thermal runaway characteristics on NCM lithium-ion batteries triggered by local heating under different heat dissipation conditions. *Appl. Therm. Eng.* **2019**, *159*, 113847.
20. An, Z.; Jia, L.; Wei, L.; Yang, C. Numerical modeling and analysis of thermal behavior and Li⁺ transport characteristic in lithium-ion battery. *Int. J. Heat Mass Transf.* **2018**, *127*, 1351–1366. [[CrossRef](#)]
21. Gamma Technologies. *GT-AutoLion User Manual*; Gamma Technologies: Westmont, IL, USA, 2019.
22. Butler, K.L.; Ehsani, M.; Kamath, P. A Matlab-Based Modeling and Simulation Package for Electric and Hybrid Electric Vehicle Design. *IEEE Trans. Veh. Technol.* **1999**, *48*, 1770–1778. [[CrossRef](#)]
23. Astaneh, M.; Andric, J.; Löfdahl, L.; Maggiolo, D.; Stopp, P.; Moghaddam, M.; Chapuis, M.; Ström, H. Calibration Optimization Methodology for Lithium-Ion Battery Pack Model for Electric Vehicles in Mining Applications. *Energies* **2020**, *13*, 3532. [[CrossRef](#)]
24. Wimmer, J.; Papadimitriou, I.; Luo, G. CAE Method for linking electrochemical Lithium-ion models into integrated system-level models of electrified vehicles. *SAE Tech. Pap.* **2018**, *1*, 1414. [[CrossRef](#)]
25. Sripad, S.; Viswanathan, V. Evaluation of Current, Future, and Beyond Li-Ion Batteries for the Electrification of Light Commercial Vehicles: Challenges and Opportunities. *J. Electrochem. Soc.* **2017**, *164*, E3635–E3646. [[CrossRef](#)]
26. Saw, L.H.; Ye, Y.; Tay, A.A.O. Electrochemical–thermal analysis of 18650 Lithium Iron Phosphate cell. *Energy Convers. Manag.* **2013**, *75*, 162–174. [[CrossRef](#)]
27. Yuan, Q.; Zhao, F.; Wang, W.; Zhao, Y.; Liang, Z.; Yan, D. Overcharge failure investigation of lithium-ion batteries. *Electrochimica Acta* **2015**, *178*, 682–688. [[CrossRef](#)]
28. Jaguemont, J.; Boulon, L.; Dube, Y. A comprehensive review of lithium-ion batteries used in hybrid and electric vehicles at cold temperatures. *Appl. Energy* **2016**, *164*, 99–114. [[CrossRef](#)]
29. Zhang, G.; Cao, L.; Ge, S.; Wang, C.Y.; Shaffer, C.E.; Rahn, C.D. In Situ Measurement of Radial Temperature Distributions in Cylindrical Li-Ion Cells. *J. Electrochem. Soc.* **2014**, *161*, A1499–A1507. [[CrossRef](#)]

Publisher’s Note: MDPI stays neutral with regard to jurisdictional claims in published maps and institutional affiliations.



© 2020 by the authors. Licensee MDPI, Basel, Switzerland. This article is an open access article distributed under the terms and conditions of the Creative Commons Attribution (CC BY) license (<http://creativecommons.org/licenses/by/4.0/>).